

RESEARCH ARTICLE

Modelling the influence of soil moisture on the Turkana jet

Joshua Talib¹  | Christopher M. Taylor^{1,2}  | Cornelia Klein¹  | James Warner³  |
Callum Munday⁴  | Sonja Folwell¹  | Cristina Charlton-Perez³ 

¹UK Centre for Ecology and Hydrology, Wallingford, UK

²National Centre for Earth Observation, Wallingford, UK

³UK Met Office, Exeter, UK

⁴University of Oxford, Oxford, UK

Correspondence

Joshua Talib, European Centre for Medium-Range Weather Forecasts, Reading, RG2 9AX, UK.

Email: joshua.talib@ecmwf.int

Funding information

Foreign, Commonwealth and Development Office, Grant/Award Number: 201880; Department for Science, Innovation & Technology; Natural Environment Research Council, Grant/Award Numbers: NE/X006247/1, NE/X017419/1, NE/X019063/1

Abstract

Low-level jets (LLJs) are sensitive to continental-scale pressure gradients. Soil moisture influences these gradients by altering turbulent flux partitioning and near-surface temperatures, thereby affecting LLJ characteristics. The Turkana jet, a strong southeasterly LLJ flowing through a channel between the Ethiopian and East African Highlands, is an important feature of the East African water cycle. Previous work has shown that the jet is sensitive to soil-moisture-induced pressure gradients driven by the Madden–Julian oscillation. Here, we build on this finding through using convection-permitting UK Met Office Unified Model simulations to isolate the role of soil moisture in shaping jet characteristics. Modelling experiments reveal that the Turkana jet is highly sensitive to soil-moisture-induced temperature gradients across the channel's exit. Prescribing realistic dry soils intensifies the local surface-induced thermal low and strengthens the jet. A maximum jet sensitivity of up to $8 \text{ m} \cdot \text{s}^{-1}$ occurs when comparing dry and wet surface states within 750 km downstream of the exit, highlighting the significant influence of soil moisture on jet dynamics, given typical speeds of $8\text{--}14 \text{ m} \cdot \text{s}^{-1}$. The impact of soil moisture on the jet is most pronounced when synoptic forcing is weak and skies are clear. Notably, despite a substantial impact on LLJ strength, we find a minor sensitivity of the vertically integrated moisture transport. We speculate that this minimal sensitivity is linked to model errors in the representation of boundary-layer turbulence, which affects midtropospheric moisture and the strength of elevated nocturnal inversions. This study highlights that the Turkana channel is a hotspot for surface–jet interactions, due to the strong sensitivity of surface fluxes to soil moisture near a topographically constrained LLJ. Future research should continue examining surface-driven predictability, particularly in regions where land–atmosphere interactions influence dynamical atmospheric conditions, and evaluate such processes in weather prediction models.

KEYWORDS

convection, convection-permitting simulations, East Africa, land surface, low-level jets, soil moisture–atmosphere feedbacks

This is an open access article under the terms of the [Creative Commons Attribution](https://creativecommons.org/licenses/by/4.0/) License, which permits use, distribution and reproduction in any medium, provided the original work is properly cited.

© 2025 The Author(s). *Quarterly Journal of the Royal Meteorological Society* published by John Wiley & Sons Ltd on behalf of Royal Meteorological Society.

1 | INTRODUCTION

Low-level jets (LLJs) play a key role in regulating continental-scale moisture transport, influencing regional moisture budgets and local precipitation patterns across the globe (Berg *et al.*, 2015; Chen & Tomassini, 2015; Correa *et al.*, 2024; Findlater, 1969; Montini *et al.*, 2019; Munday *et al.*, 2023b; Parker *et al.*, 2005; Stensrud, 1996). Among these, the Turkana jet, a strong southeasterly LLJ flowing through a channel between the Ethiopian and East African Highlands (Kinuthia, 1992; Kinuthia & Asnani, 1982; Munday *et al.*, 2022), modulates moisture transport between coastal East Africa and continental Central Africa (Munday *et al.*, 2021, 2023b; Nicholson, 2016; Viste & Sorteberg, 2013). Given that the Turkana jet influences precipitation characteristics across East Africa (King *et al.*, 2021; Munday *et al.*, 2021; Talib *et al.*, 2023; Vizy & Cook, 2019), understanding the drivers of jet variability is of utmost importance. This understanding is especially crucial in light of recent rainfall extremes (Funk *et al.*, 2023; Kilavi *et al.*, 2018; Lyon, 2014; Palmer *et al.*, 2023; Wainwright *et al.*, 2021) and low-skilled precipitation predictions (Cafaro *et al.*, 2021; MacLeod, 2018; Nicholson, 2014; Walker *et al.*, 2019). Building on several studies highlighting the impact of soil moisture gradients on LLJ dynamics (Campbell *et al.*, 2019; Chen & Dominguez, 2024; Correa *et al.*, 2024; Talib *et al.*, 2022), and more specifically on evidence that intraseasonal soil moisture variations impact Turkana jet characteristics (Talib *et al.*, 2023), we here isolate soil-moisture-driven Turkana jet variations using high-resolution convection-permitting modelling experiments.

Radiosonde observations show that the Turkana jet typically peaks between 200 and 500 m above the surface with average speeds of 10–14 m · s⁻¹ (Kinuthia, 1992; Kinuthia & Asnani, 1982; Munday *et al.*, 2022). However, jet characteristics vary substantially across space and time. For instance, maximum jet speeds of up to 30 m · s⁻¹ have been observed (Kinuthia, 1992). Observations of higher jet speeds across narrower parts of the channel (Kinuthia, 1992), alongside modelling experiments (Indeje *et al.*, 2001; Munday *et al.*, 2023b; Warner *et al.*, 2024), indicate that, to first order, the shape of the Turkana channel controls LLJ characteristics through a Bernoulli forcing. Although modelling efforts demonstrate that a fine model grid is required to correctly capture orographic processes and jet dynamics (Warner *et al.*, 2024), an improved understanding of other environmental drivers is key to improving jet forecasts. Large-scale circulation patterns, such as the monsoon flow from the Indian Ocean and subsidence from the overturning Walker circulation, as well as cross-channel temperature gradients (Hartman, 2018; Talib *et al.*, 2023; Vizy & Cook, 2019), modulate jet

intensity by altering continental-scale pressure patterns (Hartman, 2018; Talib *et al.*, 2023; Vizy & Cook, 2019). For example, the jet is most intense in September when the Somali jet advects relatively cool air to East Africa's coastal regions and increases the along-channel temperature gradient (Hartman, 2018). Surface–atmosphere interactions also affect temperature and pressure gradients, which in turn affect jet speeds (Parish & Oolman, 2010; Talib *et al.*, 2023). These interactions are critical in driving a nocturnal jet maximum (Hartman, 2018; Munday *et al.*, 2024; Nicholson, 2016; Parish & Oolman, 2010), with the most widely accepted mechanism suggesting that strong daytime coupling between the boundary layer and turbulent surface fluxes inhibits jet intensification. After sunset, as surface turbulent fluxes minimise and the boundary layer diminishes, surface–atmosphere decoupling allows the jet to intensify (Hartman, 2018; Nicholson, 2016). Additional mechanisms explaining the nocturnal jet maximum include katabatic winds driven by enhanced cooling at higher altitudes (Nicholson, 2016; Parish & Oolman, 2010) and elevated nocturnal inversions that prevent the upward mixing of momentum (Munday *et al.*, 2024). Most studies that have previously investigated the role of land–atmosphere interactions in driving jet variability have relied on observations and atmospheric reanalyses. To fully tease out the importance of land–atmosphere interactions on jet characteristics requires idealised modelling experiments in which spatial and temporal variability in surface characteristics is prescribed throughout.

In water-limited regions, where the partitioning of surface turbulent fluxes is sensitive to surface characteristics, variations in surface conditions can modulate LLJs by altering large-scale pressure gradients (Campbell *et al.*, 2019; Chug & Dominguez, 2019; Correa *et al.*, 2024; Ferguson *et al.*, 2020; Talib *et al.*, 2022). Surface drying, for example, enhances sensible heat flux (Berg *et al.*, 2014; Gallego-Elvira *et al.*, 2016; Holton, 1967; Koster *et al.*, 2009; Miralles *et al.*, 2012; Schwingshackl *et al.*, 2017; Teuling *et al.*, 2006), modifies regional pressure gradients by promoting a thermal low circulation (Berg *et al.*, 2017; Chen & Dominguez, 2024; Grimm *et al.*, 2007; Talib *et al.*, 2021, 2022), and, when near an LLJ, alters jet characteristics (Campbell *et al.*, 2019; Chen & Dominguez, 2024; Chug & Dominguez, 2019; Correa *et al.*, 2024; Ferguson *et al.*, 2020; Talib *et al.*, 2022). Focusing specifically on the Turkana jet, Talib *et al.* (2023) found that soil moisture variations associated with precipitation anomalies driven by the Madden–Julian oscillation (MJO; Madden & Julian, 1994; Mutai & Ward, 2000; Pohl & Camberlin, 2006; Berhane & Zaitchik, 2014) enhance the along-channel temperature gradient and intensify geostrophic winds. Notably, they found soil-moisture-induced turbulent flux changes at

the Turkana channel's exit to be primarily responsible for the surface-driven modulation of jet characteristics. Their analysis suggests that, on average, 10%–12% of anomalous jet speeds during active MJO events are attributable to rainfall-driven surface changes. Building on this work, which relied on observations and reanalyses, we develop a modelling framework that isolates the role of soil moisture at the channel's exit in controlling jet characteristics.

Most research on the impact of soil moisture on atmospheric conditions in Africa has focused on the initiation and development of deep convection (Klein & Taylor, 2020; Pielke, 2001; Taylor, 2015; Taylor *et al.*, 2007). Furthermore, studies examining surface-driven predictability often emphasise local thermodynamic improvements rather than dynamical atmospheric changes. For instance, whereas multimodel comparison studies demonstrate enhanced subseasonal temperature and precipitation predictions with improved soil moisture initialisation (Dirmeyer *et al.*, 2018; Koster *et al.*, 2006, 2011), these studies primarily focus on localised improvements. In this study we exploit the capability of conducting model sensitivity experiments with prescribed soil moisture to investigate soil-moisture-driven dynamical atmospheric changes, demonstrating their potential to enhance forecast accuracy. Such experiments are particularly novel as they enable the isolation of soil-moisture-driven atmospheric dynamics in a region that remains underexplored scientifically. We also take considerable care to introduce soil moisture changes that reflect realistic variability, in contrast to previous modelling studies that imposed extreme surface conditions (e.g., wilting point or saturation; Gaertner *et al.*, 2010; Cioni & Hohenegger, 2017; Chen & Dominguez, 2024). Moreover, taking note of inadequate simulations of the Turkana jet at low model resolutions (King *et al.*, 2021; Oscar *et al.*, 2022), and following the recommendation of using a maximum grid spacing of 4.4 km to capture the impacts of local orography and elevated temperature inversions on the jet (Warner *et al.*, 2024), we specifically investigate the influence of soil moisture on the Turkana jet using simulations with a 4.4 km horizontal resolution.

The structure of this study is organised as follows: Section 2 is divided into two parts. The first part (Section 2.1) outlines the observations and atmospheric reanalyses used, and the second part (Section 2.2) describes the modelling experiments performed. In Section 2.2 we provide an overview of the atmospheric model (Section 2.2.1), detail the methodology for initialising soil moisture (Section 2.2.2), outline the selection of our three case studies (Section 2.2.3), and describe the experimental design (Section 2.2.4). The results of this study are presented in Section 3 and include a comparison of control simulations with observations and atmospheric reanalyses (Section 3.1), in addition to analysis examining the sensitivity of the Turkana jet to soil moisture perturbations (Sections 3.2 and 3.3). Lastly, Sections 4 and 5 close the article with the discussion and conclusions respectively.

2 | METHODOLOGY

2.1 | Observational datasets

In this work, we use observations and atmospheric reanalyses to identify suitable case studies and assess simulation output. Table 1 provides an overview of all observational datasets utilised. Focusing on satellite-based observations, which are used to support the selection of modelling case studies, we use precipitation data from the Climate Hazards Group Infrared Precipitation with Stations (CHIRPS) product (Funk *et al.*, 2015), as well as soil moisture anomalies from the European Space Agency Climate Change Initiative (ESA CCI) combined soil moisture product version 8.1 (Dorigo *et al.*, 2017; Gruber *et al.*, 2017, 2019; van der Schalie *et al.*, 2023). Daily-accumulated precipitation on a 0.05° latitude–longitude grid from CHIRPS is derived through combining satellite-based infrared measurements with rainfall gauge totals (Funk *et al.*, 2015). Meanwhile, the ESA CCI combined soil moisture product utilises four active and 10 passive microwave-based instruments. It also uses a global land data assimilation system (GLDAS; Rodell *et al.*, 2004) to

TABLE 1 Details of observational and reanalysis datasets used in this study.

Variable	Data source	Time span	Resolution		Reference
			Spatial (°)	Temporal	
Precipitation	CHIRPS	1981–2020	0.05	Daily	Funk <i>et al.</i> (2015)
Surface soil moisture	ESA CCI	1981–2022	0.25	Daily	Dorigo <i>et al.</i> (2017)
Atmospheric conditions	ERA5	2017–2023	0.25	Hourly	Hersbach <i>et al.</i> (2019)
Atmospheric conditions	RIFTJet radiosondes	March 26–April 23, 2021	N/A	Three-hourly	Munday <i>et al.</i> (2022)

Abbreviations: CHIRPS: Climate Hazards Group Infrared Precipitation with Stations; ESA CCI: European Space Agency Climate Change Initiative; ERA5: European Centre for Medium-range Weather Forecasts Reanalysis v5; RIFTJet: Radiosonde Investigation for the Turkana Jet.

obtain a consistent climatology (Gruber *et al.*, 2019). There is no common definition for the surface soil moisture depth examined by microwave-based instruments (Dorigo *et al.*, 2017); however, it is generally assumed to be in the range of 2 to 5 cm (Ulaby, 1982).

Hourly reanalysis data from the European Centre for Medium-range Weather Forecasts Reanalysis v5 (ERA5) (Copernicus Climate Change Service (C3S), 2017; Hersbach *et al.*, 2020) is also used to support the selection of case studies. Additionally, ERA5 data are used for model initialisation and creating regional boundary conditions. ERA5, computed using four-dimensional variational data assimilation and cycle 41r2 of the Integrated Forecasting System, provides a detailed record of the global atmosphere, land, and ocean waves (Hersbach *et al.*, 2018, 2019). In this study we use ERA5 data at a 0.25° latitude–longitude resolution during the years 2017 to 2023, the same years when sensitivity experiments can be performed (Section 2.2.2). For most of this study we refer to the time of day in reference to coordinated universal time (UTC). The local time zone, East Africa Time (EAT), is 3 hr ahead of UTC.

Alongside using CHIRPS and ERA5 to assess model integrations, we also take advantage of radiosonde data from the Radiosonde Investigation for the Turkana Jet (RIFTJet) observation campaign (Munday *et al.*, 2022). Between March 26 and April 23, 2021, radiosondes were launched from Marsabit (2.3395° N, 37.9735° E; 1,337 m; denoted by the green cross in Figure 1a), a town located near the entrance of the Turkana channel, every 3 hr. Utilising in-situ jet observations improves our evaluation of simulated jet conditions, as reanalyses and coarse-resolution climate models typically underestimate jet intensities and fail to resolve elevated inversions above the jet itself (Munday *et al.*, 2023a; Oscar *et al.*, 2022). Our use of RIFTJet observations to evaluate simulations builds upon previous work investigating the impact of model resolution in simulating Turkana jet characteristics (Warner *et al.*, 2024). However, regional simulations in Warner *et al.* (2024) are bounded by model output from the global UK Met Office (UKMO) operational model, whereas our simulations are bounded by ERA5. In line with Warner *et al.* (2024), we evaluate simulation data at 37.9535° E, 2.3595° N, which assumes a 0.022° displacement of the radiosonde both northwards and westwards during its ascent from the surface to 800 hPa.

2.2 | Modelling experiments

2.2.1 | Atmospheric model

To isolate the influence of soil moisture perturbations on jet characteristics, we perform regional

convection-permitting simulations of the UKMO Unified Model (MetUM) coupled to the Joint UK Land Environment Simulator (JULES; Best *et al.*, 2011; Clark *et al.*, 2011). Initial atmospheric and hourly lateral boundary conditions for each simulation are sourced from ERA5 (Copernicus Climate Change Service (C3S), 2017; Hersbach *et al.*, 2020) at a horizontal resolution of 0.25° longitude \times 0.25° latitude.

Regional MetUM simulations across an East African domain (20 – 52° E longitude, -5.0 to $+20^\circ$ N latitude; domain shown in Figure 1) are integrated using a tropical version of the Regional Atmosphere and Land configuration version 2 (RAL2-T; Bush *et al.*, 2023). RAL2-T is an iteration on a previous tropical atmospheric model (RAL1-T; Bush *et al.*, 2020), with minor differences including the addition of three prognostic fields (liquid fraction, ice fraction, and mixed-phase fraction) in the large-scale cloud scheme (Bush *et al.*, 2023). All regional simulations are performed for 240 hr (10 days) with a 2-min atmospheric time step. The simulation length of 10 days provides a sufficient sample size of nocturnal jet conditions, enabling the analysis of its mean evolution and sensitivity to soil moisture changes. Furthermore, this simulation length allows for the investigation of accumulated atmospheric anomalies and provides valuable insight into soil moisture–jet interactions on time-scales comparable to the MJO. All regional simulations are performed with a horizontal grid spacing of 0.04° (≈ 4.4 km), 80 model levels extending up to 38.5 km, and an explicit representation of convection. Additionally, only lakes larger than 250 km² are resolved. JULES has four soil layers, with depths of 0.1, 0.25, 0.65, and 2.0 m. In our regional model configuration, there is no coupling between the atmosphere and ocean. Sea-surface temperatures, as well as lake temperatures, are prescribed using surface temperatures from ERA5. All simulations are prescribed with climatological aerosols. Our regional model configuration is consistent with the current pan-African UKMO operational model (Cafaro *et al.*, 2021; Fletcher *et al.*, 2022), and with recent work investigating sensitivities of the simulated East African climate to model configuration changes (Warner *et al.*, 2023, 2024).

2.2.2 | Initialisation of soil moisture

Given our emphasis on understanding soil-moisture–atmosphere interactions, considerable effort has been taken to ensure the appropriate initialisation of soil moisture. In each simulation, initialised soil moisture values are based on data from the global UKMO operational model. For example, in simulations commencing at 0000 UTC (0300 h EAT) on April 11, 2021, soil moisture is

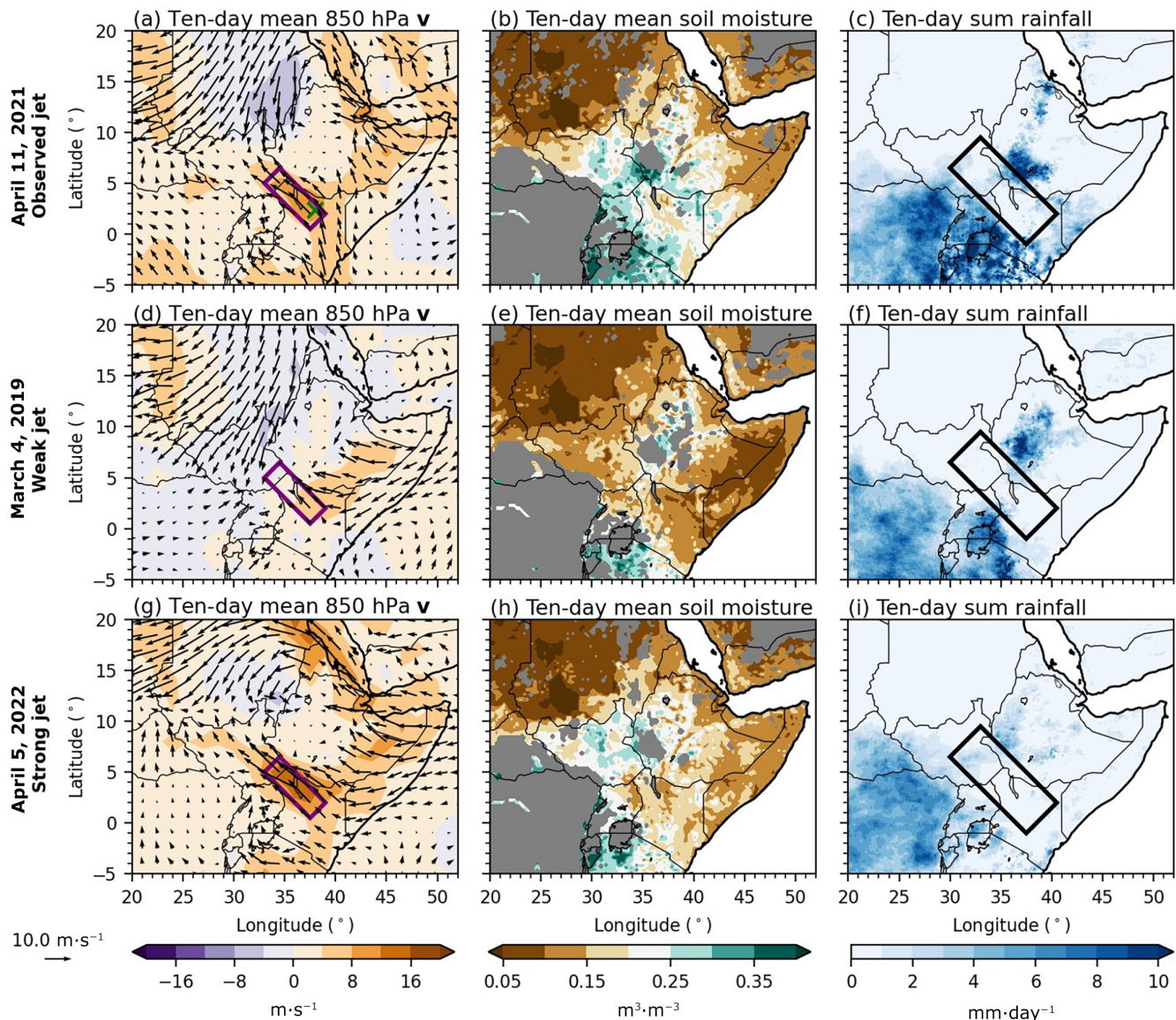


FIGURE 1 The 10-day mean of (a, d, g) the channel-orientated (filled) and horizontal (arrows) wind ($\text{m} \cdot \text{s}^{-1}$) at 850 hPa, (b, e, h) the European Space Agency Climate Change Initiative surface soil moisture ($\text{m}^3 \cdot \text{m}^{-3}$); (c, f, i) the 10-day rainfall accumulation ($\text{mm} \cdot \text{day}^{-1}$) during each of the chosen case studies. (a)–(i) Environmental conditions for 10-day case studies commencing on (a–c) April 11, 2021, (d–f) March 3, 2019, and (g–i) April 5, 2022. To improve visualisation, horizontal wind components are only shown for every fourth grid point ($\approx 1.0^\circ$). The purple transect in panels (a), (d), and (g) denotes the area used to identify periods with strong and weak jet conditions, and the black transect in panels (c), (f), and (i) denotes the area used to quantify rainfall in the periphery of the Turkana jet (Supporting Information Figure S1). The green cross in (a) denotes the town of Marsabit, where radiosondes were launched from during the Radiosonde Investigation for the Turkana Jet campaign. [Colour figure can be viewed at [wileyonlinelibrary.com](https://onlinelibrary.wiley.com)]

initialised from operational forecast values commencing at the same hour. Section S1 in the Supporting Information provides specific details regarding the regridding of soil moisture data from the UKMO operational model to our high-resolution model grid. We follow the same regridding technique that is currently used operationally at the UKMO.

Assimilated observations used to compute initial UKMO soil moisture include ground-based measurements

of air temperature and specific humidity at 1.5 m, as well as satellite-derived soil wetness data from advanced scatterometer (ASCAT) observations (Dharssi *et al.*, 2011; Gómez *et al.*, 2020). Gómez *et al.* (2020) outline the process of assimilating ASCAT-derived soil wetness into the MetUM, including bias correction of the observations and converting the soil wetness index into volumetric soil moisture. The assimilation of multiple observational products results in a more accurate initialisation of soil

moisture compared with relying solely on previous operational forecasts, leading to improved predictions of surface heat fluxes and near-surface atmospheric conditions. In our modelling set-up, soil moisture evolves freely after initialisation unless specified otherwise.

2.2.3 | Case study selection

Three initialisation dates were selected to examine the impact of soil moisture anomalies on jet characteristics. Since a substantial fraction of annual rainfall occurs during the long rains season (March to May; Nicholson, 2017; Palmer *et al.*, 2023), a period characterised by low forecast skill (Cafaro *et al.*, 2021; de Andrade *et al.*, 2021; Nicholson, 2014; Walker *et al.*, 2019), we focused on case studies initialised within these months. Additionally, to ensure consistency with the global UKMO operational model (section 2.2.2; Walters *et al.*, 2017; Gómez *et al.*, 2020) and due to the availability of operational soil moisture data, our case studies were restricted to the years 2017 to 2023.

Two metrics guided our selection of initialisation dates:

1. The 10-day rainfall averages in the periphery of the Turkana channel, defined by the corner points (-1.0° N, 37.5° E), (6.5° N, 30.0° E), (9.5° N, 33.0° E) and (2.0° N, 40.5° E) (black transects in Figure 1).
2. The 10-day averages of the nocturnal channel-orientated wind speed (bearing 315°) in the Turkana channel, defined by the corner points (0.5° N, 37.5° E), (5.0° N, 33.0° E), (6.5° N, 34.5° E), and (2.0° N, 39.0° E) (purple transects in Figure 1).

Our computation of 10-day averages is motivated by simulation length, as detailed in Section 2.2.1. Regarding rainfall, we decided to focus on 10-day periods with minimal precipitation in the periphery of the Turkana channel to minimise interactions between deep convection and the jet itself. Supporting Information Figure S1a illustrates average 10-day precipitation rates against 10-day mean nocturnal jet speeds. Though weaker jet speeds are associated with greater rainfall in the Turkana channel,

consistent with King *et al.* (2021), we identify several 10-day periods that are characterised by strong or weak jet conditions with minimal rainfall. After considering jet speeds below and exceeding the 5th and 95th percentile respectively (Supporting Information Figure S1b,c), we selected March 4, 2019, and April 5, 2022, as our case study initialisation dates to represent weak and strong jet conditions respectively (red squares in Supporting Information Figure S1b,c). These dates allow us to investigate soil-moisture–jet interactions during weak and strong jet conditions respectively while minimising the influencing of convection on the jet.

Additionally, we perform a set of simulations initialised on April 11, 2021, the date with the lowest 10-day precipitation accumulation around the Turkana jet during the RIFTJet campaign (Section 2.1). This date is also characterised by the strongest nocturnal jet observed during the campaign (Munday *et al.*, 2022), although the 10-day average jet speed was similar to the rest of the campaign (Supporting Information Figure S1d). By performing simulations with a start date in the RIFTJet campaign, we can compare model outputs with radiosonde observations, in addition to atmospheric reanalyses. It is also important to note that our simulation initialised on April 11, 2021, coincides with phase 7 active MJO conditions, characterised by dry conditions across East Africa (Berhane & Zaitchik, 2014; Mutai & Ward, 2000; Pohl & Camberlin, 2006; Talib *et al.*, 2023), whilst March 4, 2019, and April 5, 2022, corresponded to an active MJO in phase 3 (wet) and an inactive MJO respectively. For the remainder of this study, we refer to case studies initialised on April 11, 2021, March 4, 2019, and April 5, 2022, as “observed”, “weak”, and “strong” jet conditions respectively. Table 2 summarises all case study attributes, including an overview of atmospheric characteristics. Figure 1 shows 10-day means of 850 hPa ERA5 horizontal wind and ESA CCI surface soil moisture, as well as 10-day precipitation accumulations from CHIRPS for each chosen case study. As can be inferred from the figure, these case studies allow us to examine soil-moisture–jet interactions under varying jet characteristics and surface environments, while minimising the effects of jet–convection interactions.

TABLE 2 Details of 10-day case studies conducted in this study including 10-day averages of observed rainfall rates in the periphery of the Turkana channel and channel-orientated wind speeds within the channel itself.

Initialisation date	Case study name	Average rainfall rate ($\text{mm} \cdot \text{day}^{-1}$)	Average wind speed ($\text{m} \cdot \text{s}^{-1}$)	Dominant MJO phase
April 11, 2021	Observed jet	1.2	7.2	7
March 4, 2019	Weak jet	0.4	2.6	3
April 5, 2022	Strong jet	0.6	9.9	Neutral

Abbreviation: MJO: Madden–Julian oscillation.

2.2.4 | Experiment design

For each case study we perform multiple MetUM simulations. We first compute atmospheric integrations with free-running, interactive soil moisture. For the rest of this study, these atmospheric integrations will be referred to as “control” simulations and denoted with a “C” label. These simulations enable us to evaluate simulated atmospheric conditions against radiosonde observations and reanalyses.

To isolate the influence of soil moisture on the Turkana jet, we perform a series of sensitivity experiments where soil moisture is prescribed across all four JULES soil layers within the simulation domain. To fix soil moisture within the model domain, we define a spatially varying “soil moisture scaling factor” (Figure 2a). At grid points where the scaling factor is equal to one, soil moisture is reset

to the prescribed value at the end of every time step and therefore remains constant throughout the entire 10-day simulation. At other grid points where the scaling factor is equal to zero, soil moisture can vary and is interactive with the atmospheric model.

Here, we primarily focus on isolating the importance of soil moisture within the channel’s exit, as this area was identified as a hotspot for soil-moisture–atmosphere interactions on MJO time-scales (Talib *et al.*, 2023). To prescribe soil moisture within the Turkana channel’s exit region, we define a sector that is between the angles of 290° and 340° , and is centred at 4.5° N latitude and 35.0° E longitude. After excluding the first 100 km from the central point, we prescribe soil moisture with a sector length of 500, 750, and 1,000 km. Figure 2a shows the scaling factor when prescribing soil moisture within 500 km of the Turkana channel’s exit, and Figure 2b shows prescribed

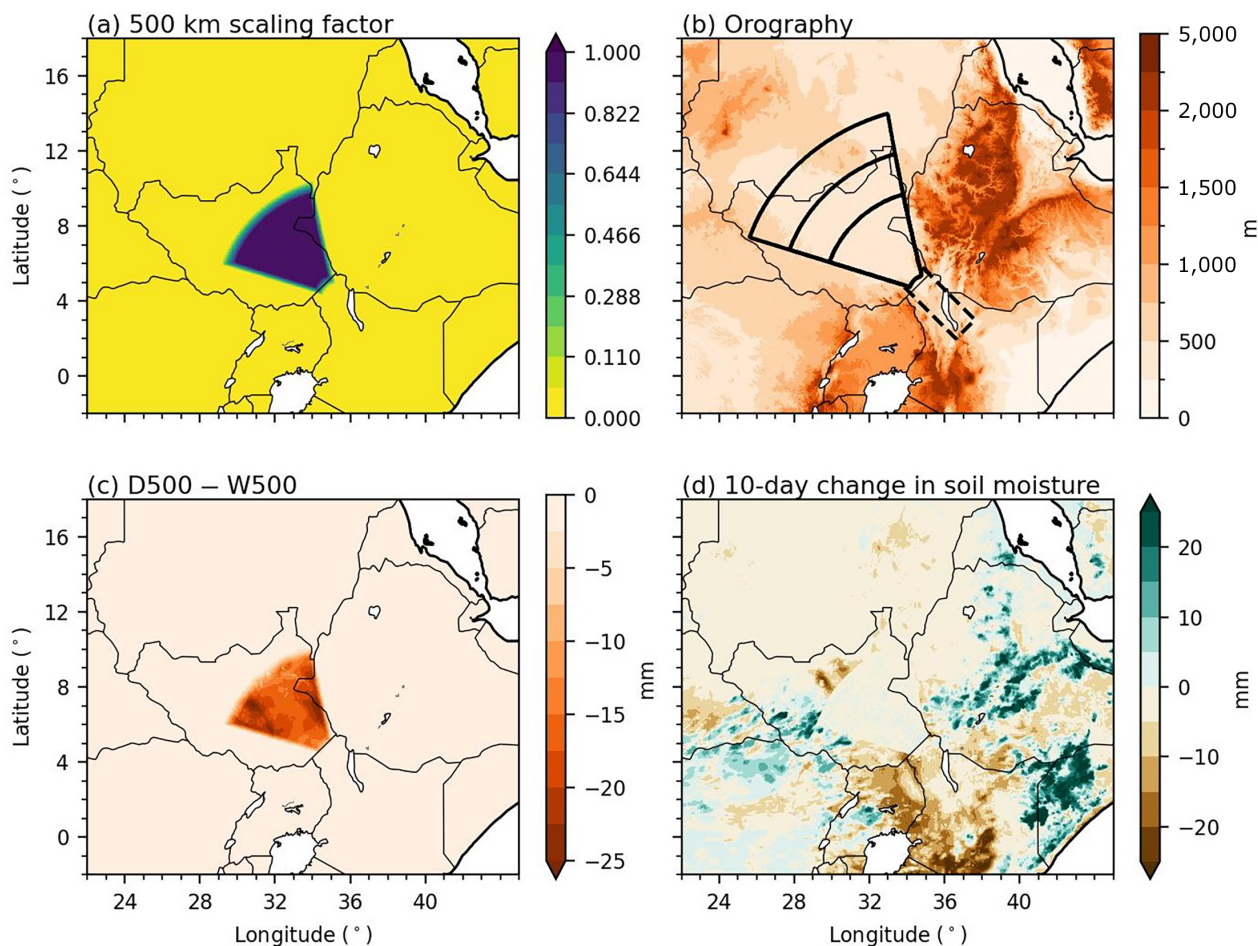


FIGURE 2 (a) The prescribed soil moisture scaling factor for all soil depths in 500 km experiments. (b) Orography (filled, m) and black lined contours showing the perimeter of soil moisture scaling factors equal to 1.0 for simulations with a sector extent of 500, 750, and 1,000 km. The dashed black rectangle shows the region used to prescribe soil moisture in the Turkana channel. (c) The difference in initial surface soil moisture (mm) between dry (D500) and wet (W500) simulations with prescribed soil moisture within 500 km of the Turkana channel’s exit. (d) The 10-day change in surface soil moisture (mm) over the course of the D500 simulation commencing on April 11, 2021. [Colour figure can be viewed at [wileyonlinelibrary.com](https://onlinelibrary.wiley.com)]

soil moisture regions with sector lengths of 500, 750, and 1,000 km within the Turkana channel's exit. In addition to defining an area where soil moisture is fixed, we define a boundary that is approximately 50 km from the edge of fixed soil moisture conditions. In this area, the scaling factor linearly reduces from one to zero. At locations with a fractional scaling factor, soil moisture is updated at every time step using a weighted-average between prescribed and interactive soil moisture. For instance, if the scaling factor is equal to 0.7, the computed soil moisture uses a weighting of 0.7 and 0.3 for prescribed and interactive soil moisture values respectively. Creating a model set-up that includes a boundary where the change between prescribed and interactive soil moisture is smoothed reduces the likelihood of strong soil moisture gradients and the possible formation of soil-moisture-driven circulations (Pielke Sr., 2001; Taylor *et al.*, 2007, 2011). We also perform sensitivity experiments where soil moisture is prescribed within the Turkana channel in addition to its exit region. The Turkana channel, shown as a dashed rectangle in Figure 2, is defined with the corner points of (5.0° N, 33.6° E), (6.0° N, 34.6° E), (3.0° N, 37.6° E), and (2.0° N, 36.6° E).

To summarise, the 10-day simulations performed for each case study are as follows.

- **Control simulation:** a baseline simulation with free-running, interactive soil moisture.
- **Dry simulations:** simulations with dry surface conditions in the channel's exit of a length scale of 500, 750, and 1,000 km.
- **Wet simulations:** simulations with wet surface conditions in the channel's exit of a length scale of 500, 750 and 1,000 km.
- **Within-channel fixed soil moisture simulations:** dry and wet simulations with fixed soil moisture within 500 km of the channel's exit and throughout the channel.

Table 3 outlines all simulations performed for each initialisation date (Table 2). The remainder of this section

describes the computation of prescribed soil moisture values and the methodology used for labelling simulations.

In this study, we carefully introduce soil moisture changes that reflect realistic variability, as captured by the UKMO operational model. Unlike previous studies that imposed extreme surface conditions (e.g., wilting point or saturation; Gaertner *et al.*, 2010; Cioni & Hohenegger, 2017; Chen & Dominguez, 2024), this approach enables a more meaningful assessment of how soil moisture variability impacts the Turkana jet and its implications for operational forecasting. To define realistic dry and wet conditions, we use soil moisture initialisations from the UKMO global operational model. Using initialisation data from 2016 to 2023, the 10th and 90th percentiles of 10-day rolling means of initialised soil moisture in March–May are used to represent dry and wet conditions respectively. Discussed in more detail in Supporting Information Section S1, operational soil moisture at an N768 resolution (0.2° longitude × 0.16° latitude) during 2016 and 2017 is interpolated to the operational resolution from 2018 onwards (N1280; 0.14° longitude × 0.09° latitude). Figure 2c shows the difference in initial surface soil moisture between dry and wet simulations when soil moisture is prescribed within 500 km of the channel's exit. Additionally, Supporting Information Figure S2 shows the difference between dry and wet surface conditions across the whole simulation domain for all four soil depths. Within the channel's exit, the most substantial soil moisture differences occur at the surface in wetland areas such as the Sudd (Figure 2c and Supporting Information Figure S2c). Reduced soil moisture within the channel's exit decreases both the surface conductivity for evaporation from bare soil (Figure S3c–e; Best *et al.*, 2011) and the efficiency of plant transpiration (Supporting Information Figure S3f–h).

The labelling of fixed soil moisture simulations includes a prefix of “D” or “W” to respectively denote dry or wet soil moisture conditions followed by the size of the soil moisture perturbation in kilometres (Table 3). For example, dry simulations with fixed soil moisture conditions of a length-scale of 500 km are labelled “D500”.

TABLE 3 Assigned simulation labels for all atmospheric integrations performed in this study. A complete set of simulations is performed for each case study (Section 2.2.3).

Treatment of soil moisture	Size of soil moisture perturbation (km)				
	0	500	750	1,000	500 plus channel
Interactive	C				
Dry		D500	D750	D1000	D500PC
Wet		W500	W750	W1000	W500PC

Simulations with fixed soil moisture in the Turkana channel, in addition to its exit, are given the suffix “PC”, shorthand for “plus channel”. To further highlight that soil moisture is fixed within a chosen region of the model domain, Figure 2d shows the total soil moisture change in the D500 simulation commencing April 11, 2021. By design, within the prescribed region the soil moisture remains constant, whereas in other locations the soil moisture is allowed to vary.

3 | RESULTS

3.1 | Evaluation of control simulations

Before examining the simulated impact of soil moisture perturbations on the Turkana jet, we first compare mean atmospheric conditions from the control simulations with satellite-derived rainfall totals and atmospheric reanalyses (Figure 3), as well as radiosonde

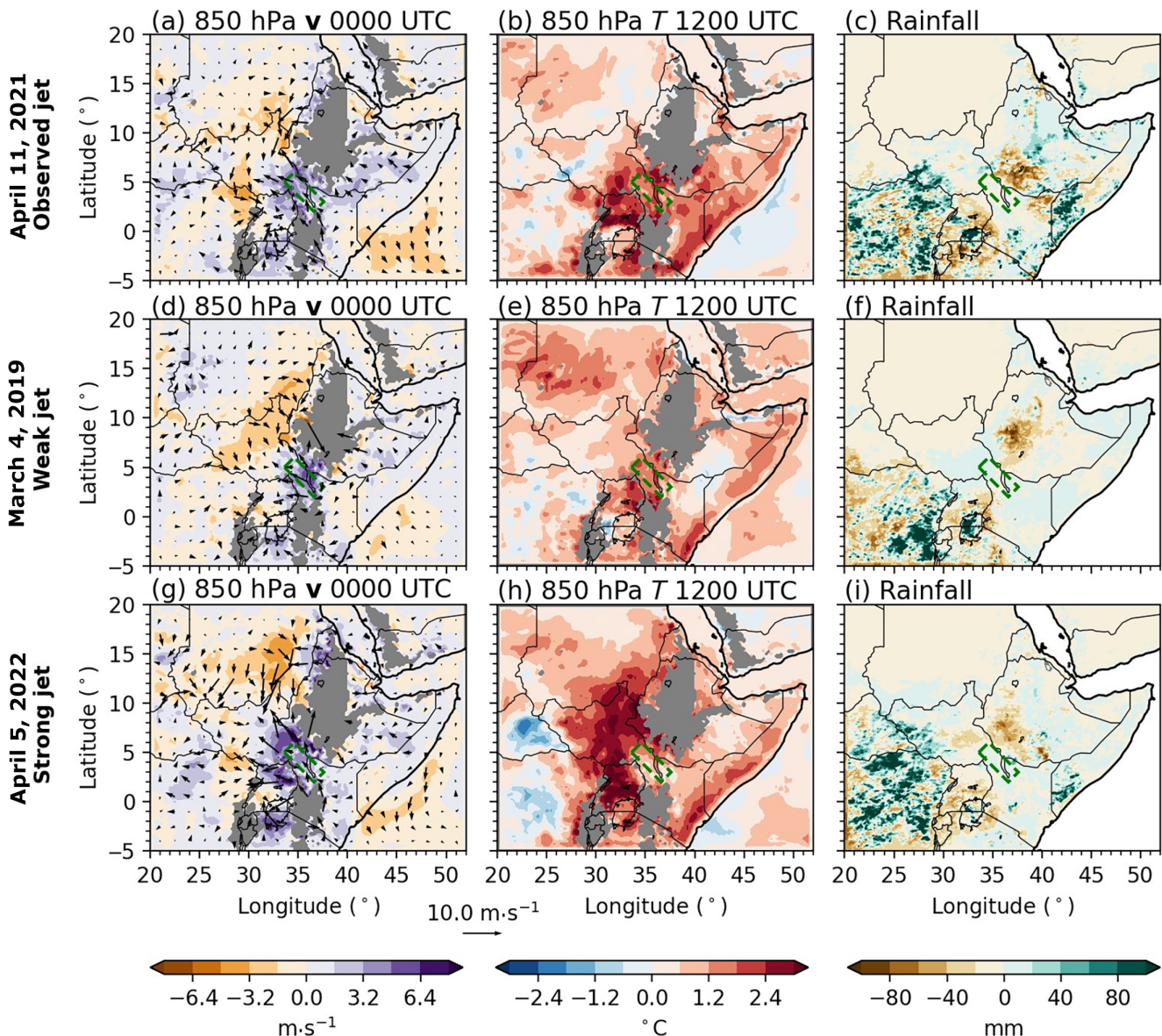


FIGURE 3 The 10-day mean differences between simulated atmospheric conditions and European Centre for Medium-range Weather Forecasts Reanalysis v5 (ERA5) 850 hPa (a, d, g) 0000 UTC/0300 h EAT channel-orientated wind speed (filled, $\text{m} \cdot \text{s}^{-1}$) and (b, e, h) 1200 UTC/1500 h EAT temperature (filled, $^{\circ}\text{C}$), as well as (c, f, i) 10-day accumulated Climate Hazards Group Infrared Precipitation with Stations (CHIRPS) rainfall data (filled, mm). To evaluate simulated conditions, model output is linearly interpolated to the grid used for ERA5 and CHIRPS data. Atmospheric differences are shown for case studies initialised on (a–c) April 11, 2021, (d–f) March 4, 2019, and (g–i) April 5, 2022. Arrows in panels (a), (d), and (g) denote horizontal wind components; these are only shown every sixth grid point ($\approx 1.5^{\circ}$) to improve visualisation. Dashed green rectangles in all panels highlight the location of the Turkana channel. [Colour figure can be viewed at [wileyonlinelibrary.com](https://onlinelibrary.wiley.com/doi/10.1002/qj.4972)]

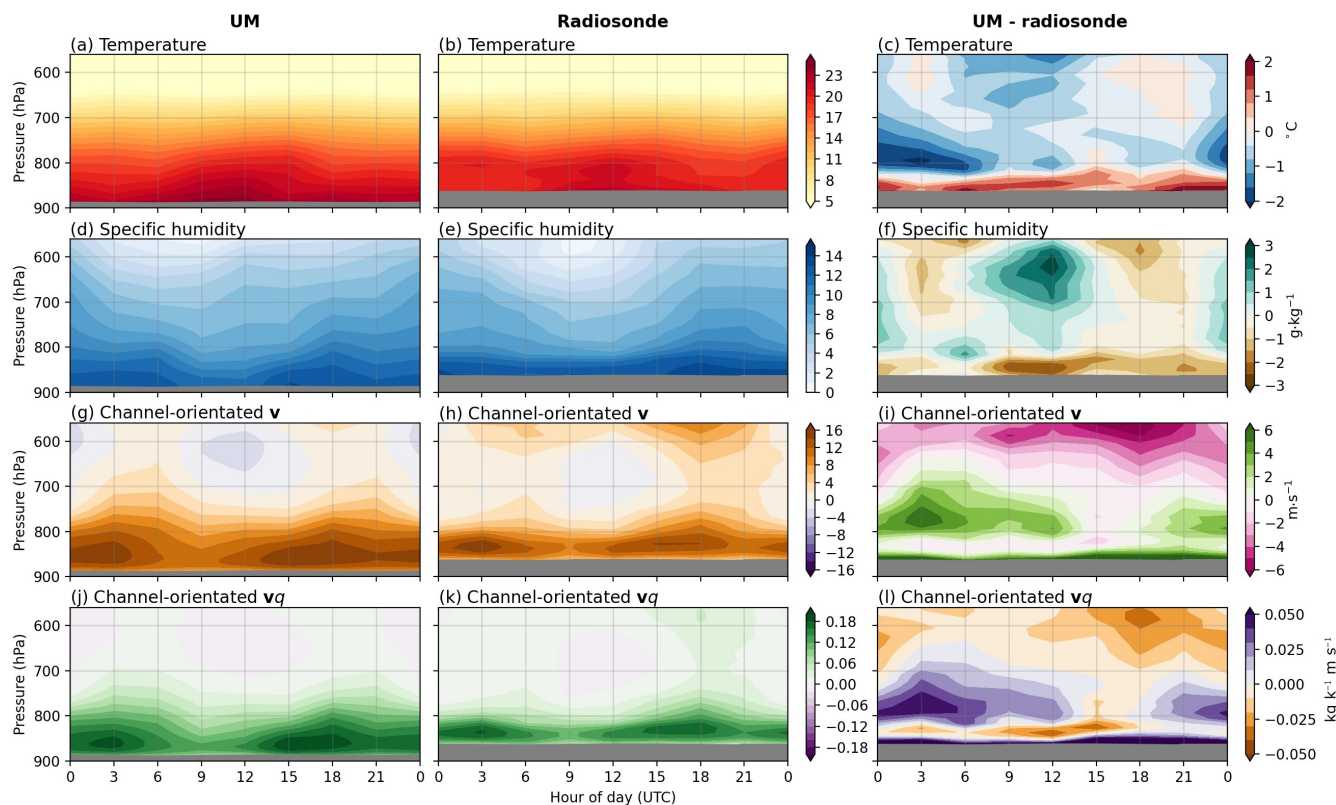


FIGURE 4 The 10-day mean diurnal cycles of atmospheric profiles in (a–c) temperature ($^{\circ}\text{C}$), (d–f) specific humidity ($\text{g} \cdot \text{kg}^{-1}$), (g–i) channel-orientated wind speed ($\text{m} \cdot \text{s}^{-1}$), and (j–l) channel-orientated moisture flux ($\text{kg} \cdot \text{kg}^{-1} \cdot \text{m} \cdot \text{s}^{-1}$). (a, d, g, j) Mean absolute values from the control simulation initialised on April 11, 2021; (b, e, h, k) mean radiosonde observations taken during the same 10-day period. (c, f, i, l) Differences between control simulations and radiosonde observations. In all panels, grey shading represents pressures greater than the 10-day minimum surface pressure, calculated at 3-hr intervals. For panels comparing simulations with observations, the minimum surface pressure between radiosonde data and UK Met Office Unified Model simulation output is used. [Colour figure can be viewed at [wileyonlinelibrary.com](https://onlinelibrary.wiley.com)]

data (Figure 4). Evaluating our control simulations is challenging owing to the limited availability of reliable observations and the inaccuracies in atmospheric reanalyses. Recent work by Munday *et al.* (2023a) highlights that reanalyses tend to underestimate jet speeds by up to $5 \text{ m} \cdot \text{s}^{-1}$, mainly due to poor representation of elevated inversions and low-tropospheric subsidence. Given these findings, and that MetUM convection-permitting simulations better capture elevated inversions (Warner *et al.*, 2024), it is unsurprising that our control simulations exhibit stronger jet speeds compared with ERA5 (Figure 3a,d,g). We also simulate stronger winds across the windward side of both the East African and Ethiopian highlands, suggesting that orographic processes simulated at finer resolutions, such as katabatic flows off steep terrains (Parish & Oolman, 2010; Vizy & Cook, 2019), strengthen wind speeds across large areas of coastal East Africa. Additionally, the largest wind differences are found during the strong jet case study commencing on April 5, 2022 (Figure 3g). We speculate that these particularly large wind differences are associated with a strong along-channel temperature

difference (Figure 3h) that enhances the along-channel pressure gradient and the Turkana jet, consistent with Hartman (2018). Further focusing on temperature, all three control simulations develop a regional-scale warm bias of up to 2.5°C relative to ERA5 (Figure 3b,e,h). Previous analysis of the MetUM model in this region showed that simulated evapotranspiration during a 10-day dry spell declines too rapidly (Gallego-Elvira *et al.*, 2019). This leads to an accelerated warming of the land surface, which in turn enhances sensible heat fluxes and raises boundary-layer temperatures. Such behaviour in the land-surface scheme likely contributes to warm atmospheric biases in our simulations. Furthermore, we hypothesise that such biases enhance the along-channel temperature gradient, which intensifies the Turkana jet and leads to similar jet speeds in both control and dry simulations (Supporting Information Figure S4).

In addition to stronger winds on the windward side of the Highlands, slower winds are simulated across South Sudan and southern areas of Sudan. This combination of positive and negative wind differences leads to

discrepancies in atmospheric convergence, particularly across wetlands in South Sudan (not shown), with implications for the vertically integrated moisture transport. However, enhanced convergence simulated in control integrations does not lead to relatively high precipitation errors when comparing simulated rainfall with CHIRPS data (Figure 3c,f,i). Further focusing on precipitation, it is unsurprising that errors in 10-day rainfall accumulations are large and maximise to approximately 100 mm across the Democratic Republic of Congo given the chaotic behaviour of deep convection. Reassuringly, however, there are minimal precipitation errors in the periphery of the Turkana channel, indicating minimal jet–convection interactions in our model simulations. We also found that the co-location of precipitation and near-surface temperatures differences across semi-arid regions (not shown) suggests strong coupling between precipitation and the near-surface atmosphere; that is, enhanced precipitation is co-located with cold temperature differences. To conclude, although our convection-permitting simulations struggle to capture the exact location of deep convective systems, the occurrence of faster channel-orientated wind speeds in our control integrations compared with ERA5 indicates that local orographic processes strengthen jet speeds for all three case studies.

Building on previous work by Warner *et al.* (2024), who evaluated MetUM convection-permitting simulations against all radiosondes released during the RIFTJet campaign, Figure 4 compares simulated diurnal cycles in temperature, specific humidity, channel-orientated wind speed, and channel-orientated moisture flux with RIFTJet radiosondes released between April 11 and April 21, 2021. We find that simulated temperatures below 800 hPa are up to 2°C warmer compared with radiosonde data (Figure 4c). In addition, although Warner *et al.* (2024) conclude that convection-permitting simulations better resolve nocturnal elevated inversions than atmospheric integrations with parametrised convection do, we both find that these inversions are still too cold by up to 2°C. Focusing on specific humidity, it is evident that the model overestimates daytime boundary-layer growth (Figure 4d,e) with large daytime (0600–1500 UTC/0900–1800 h EAT) midtropospheric wet errors of up to 3 g · kg⁻¹ (Figure 4f). Whereas humidity errors weaken during the evening (1800–2100 UTC/2100–0000 h EAT, ≈ -1 g · kg⁻¹), positive humidity biases are simulated in the latter half of the night (0000 and 0300 UTC/0300 h and 0600 h EAT). As concluded in Munday *et al.* (2022), a narrow jet predominantly confined to below 800 hPa is observed (Figure 4h). Our control integrations, on the other hand, simulate a much broader LLJ (Figure 4h) with positive nocturnal wind errors maximising to 6 m · s⁻¹ at 800 hPa (Figure 4h). Intensified channel-orientated winds

between 800 and 700 hPa lead to positive errors in the channel-orientated moisture flux (Figure 4l). As speculated by Warner *et al.* (2024), this increased depth of channel-orientated moisture fluxes may contribute to an overestimated moisture transport through the Turkana channel. In summary, our high-resolution control simulations reasonably capture the diurnal evolution of the Turkana jet, including its peak intensity, and minimal rainfall in the jet periphery. However, when analysing the simulated impact of soil moisture on the LLJ, we must keep in mind that our model configuration overestimates daytime boundary-layer growth and the depth of the nocturnal jet.

3.2 | Sensitivity of the Turkana jet to soil moisture within 500 km of the channel's exit

To begin investigating the impact of soil moisture anomalies on the Turkana jet, we focus on simulations with fixed soil moisture within 500 km of the Turkana channel's exit (Table 3, D500 and W500). Figure 5 shows 10-day mean temperature and geopotential height differences at 850 hPa between dry (D500) and wet (W500) simulations, as well as differences in channel-orientated wind speed and moisture flux. Channel-orientated diagnostics are calculated at a bearing of 315° using both horizontal wind components. Additionally, we illustrate differences in wind and moisture convergence after downscaling to a 0.5° resolution using first-order conservative regridding. Owing to well-known sub-daily variations in the thermodynamic and dynamic response to anomalous surface turbulent fluxes (e.g., Rácz & Smith, 1999; Parker *et al.*, 2005; Talib *et al.*, 2022, and discussed later) (discussed later), we show temperature and geopotential height differences at 1200 UTC/1500 h EAT, and the wind and moisture flux differences are shown at 0000 UTC/0300 h EAT. When comparing the difference between dry and wet simulations, we find that drier soils, and a reduced evaporative fraction (Supporting Information Figure S3i–k), across the lowlands of South Sudan lead to substantially warmer low-tropospheric temperatures by up to 3°C (Figure 5a–c). Low-tropospheric warming promotes a thermal low across the channel's exit, which is highlighted by a negative geopotential height difference of up to 6–7 m (Figure 5d–f) and converging low-level winds (Figure 5g–i). Consistent with observations during active MJO events (Talib *et al.*, 2023), the surface-driven heat low anomaly intensifies nocturnal channel-orientated wind speeds through the Turkana channel by up to 5 m · s⁻¹. In light of mean jet speeds of between 10 and 15 m · s⁻¹ in our control simulations (Supporting Information

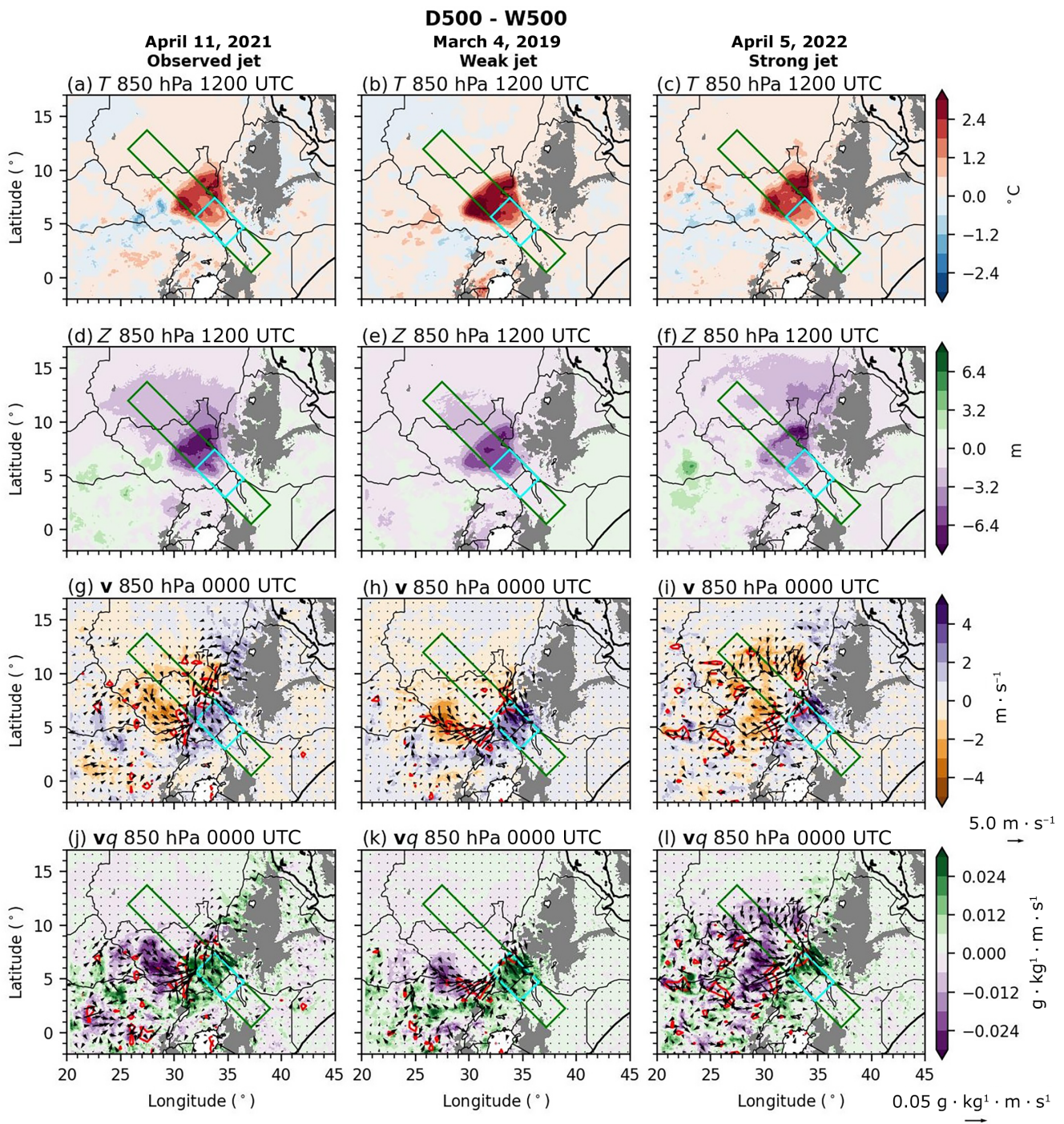


FIGURE 5 The 10-day mean atmospheric differences between D500 and W500 simulations with prescribed soil moisture within 500 km of the Turkana channel's exit: (a–c) air temperature (filled, °C) and (d–f) geopotential height (filled, m) at 1200 UTC/1500 h EAT; (g–i) channel-orientated wind speed (filled, $\text{m} \cdot \text{s}^{-1}$) and (j–l) channel-orientated moisture flux (filled, $\text{kg} \cdot \text{kg}^{-1} \cdot \text{m} \cdot \text{s}^{-1}$) at 0000 UTC/0300 h EAT. All atmospheric differences are shown at 850 hPa. Arrows in (g)–(i) denote horizontal wind components, whereas in (j)–(l) they denote horizontal moisture flux components. To improve visualisation, arrows are only shown for every 20th grid point ($\approx 0.8^\circ$). Red lined contours in (g)–(i) and (j)–(l) mark areas of wind and moisture convergence greater than $2.5 \times 10^{-5} \text{ s}^{-1}$ and $2.5 \times 10^{-7} \text{ kg} \cdot \text{kg}^{-1} \cdot \text{s}^{-1}$ respectively, after downscaling to a 0.5° resolution. Simulated atmospheric differences are shown for case studies initialised on (a, d, g, j) April 11, 2021, (b, e, h, k) March 4, 2019, and (c, f, i, l) April 5, 2022. On all panels, grey shading indicates grid points where the minimum surface pressure between D500 and W500 is smaller than 850 hPa at any time in the 10-day simulations. Green and cyan rectangles in all panels highlight the areas used for vertical cross-sections through the Turkana channel (Figure 6) and computing vertical profiles of the channel-orientated moisture flux (Figure 7) respectively. [Colour figure can be viewed at wileyonlinelibrary.com]

Figure S4), in addition to observed jet speeds of a similar magnitude (Kinuthia, 1992; Kinuthia & Asnani, 1982; Munday *et al.*, 2022), we conclude that soil moisture in the channel's exit can substantially control jet intensities. Intensified nocturnal winds when prescribing drier soils enhance low-tropospheric wind convergence across the lowlands of South Sudan (Figure 5g–i) and increase low-level channel-orientated moisture transport by up to $0.025 \text{ kg} \cdot \text{kg}^{-1} \cdot \text{m} \cdot \text{s}^{-1}$ (Figure 5j–l).

The impact of fixed soil moisture differences on the atmosphere varies vertically. To better understand this varied atmospheric response to differences in prescribed soil moisture, Figure 6 shows vertical cross-sections of 10-day mean differences between D500 and W500 in temperature, channel-orientated wind speed, specific humidity, and channel-orientated moisture flux. Additionally, wind speeds and moisture fluxes from the control simulations are displayed in lined contours. For all three case studies, prescribing dry soils leads to anomalous warming below approximately 650 hPa compared with when prescribing wet soils (Figure 6a,e,i). Cooling of up to 1.5°C is simulated in the overlying layer (650–550 hPa), consistent with previous studies that find midlevel divergence and cooling above a surface-induced thermal low (e.g., Howard & Washington, 2018; Rácz & Smith, 1999; Talib *et al.*, 2021). The soil moisture-induced thermal low promotes an overturning circulation centred over prescribed soil moisture anomalies (Figure 6b,f,j). This overturning circulation aligns with climatological patterns identified in atmospheric reanalyses (Nicholson, 2016) and supports the argument that seasonal variations in low-level thermal forcing influence jet intensity (Hartman, 2018). Between the surface and 825 hPa, channel-orientated wind speeds and moisture fluxes are enhanced for all three case studies. Above 825 hPa and up to approximately 600 hPa, the overturning circulation weakens channel-orientated wind speeds and moisture fluxes by up to $3 \text{ m} \cdot \text{s}^{-1}$ and $0.03 \text{ kg} \cdot \text{kg}^{-1} \cdot \text{m} \cdot \text{s}^{-1}$ respectively. As expected, prescribing dry soils reduces near-surface specific humidity due to reduced surface evapotranspiration (Figure 6c,g,k). However, the co-location of wind and moisture flux differences indicates that moisture transport changes are predominately controlled by wind variations.

From Figures 5 and 6 we conclude that the magnitude of the atmospheric response to differences in prescribed soil moisture is sensitive to the initialisation date chosen. For instance, surface-induced temperature perturbations reach up to 3°C under weak jet conditions, whereas, under strong jet conditions, warm temperature anomalies are advected downstream, prohibiting the build-up of surface-driven heating (Figure 6e,i). Reduced heat advection under weak jet conditions leads to a stronger

thermal gradient, and hence a more intense thermal-low circulation (Figure 6f,j). Supporting Information Figure S4 shows that under weak jet conditions we simulate a jet strengthening of approximately 65% when comparing simulations with prescribed dry or wet soils. Meanwhile, for the other two case studies, an average jet intensification of 13% to 17% is simulated. In addition to strong jet conditions reducing the amount of anomalous heat contained within the channel's exit, we speculate that large-scale synoptic variability responsible for an intense LLJ reduces the importance of surface-driven processes. This aligns with a weaker sensitivity of the nocturnal jet when the preceding daytime along-channel pressure difference is greater (Supporting Information Figure S5). Similar conclusions have been reached in studies of the LLJ across the Great Plains of the United States (Campbell *et al.*, 2019; Ferguson *et al.*, 2020); the influence of soil moisture on LLJ characteristics is significantly larger when the jet is weak or decoupled from the upper level jet stream (Burrows *et al.*, 2019; Campbell *et al.*, 2019). Though multiple studies have demonstrated that the Turkana jet is sensitive to large-scale atmospheric conditions (King *et al.*, 2021; Nicholson, 2016; Vizy & Cook, 2019), further research is needed to comprehensively quantify how the jet's sensitivity to large-scale atmospheric conditions affects surface-induced jet variations.

In general, dry soils in the Turkana channel's exit intensify the nocturnal LLJ and enhance low-tropospheric moisture transport. However, the surface-induced overturning circulation also leads to an anomalous moisture transport in the opposite direction between approximately 800 and 600 hPa (Figure 6d,h,l). To investigate the importance of this anomalous midtropospheric moisture flow in more detail, Figure 7 presents area-averaged vertical profiles of channel-orientated moisture fluxes across the immediate exit of the Turkana channel (bounded area with corner points of $(2.95^\circ \text{ N}, 34.75^\circ \text{ E})$, $(5.7^\circ \text{ N}, 32.0^\circ \text{ E})$, $(7.46^\circ \text{ N}, 33.76^\circ \text{ E})$, and $(4.71^\circ \text{ N}, 36.51^\circ \text{ E})$ denoted by cyan rectangles in Figure 5 and dashed vertical lines in Figure 6d,h,l). The figure also partitions moisture flux differences into variations driven by wind or humidity. Both dry and wet simulations exhibit a positive channel-orientated moisture flux up to approximately 400 hPa (Figure 7), with dry soils strengthening fluxes below 800 hPa and weakening them above. Consistent with the co-location of wind and moisture flux differences in Figure 6, wind changes are primarily responsible for moisture flux differences (dotted lines). Interestingly, however, midtropospheric moisture flux differences have a greater impact on vertically integrated moisture transport than low-level variations do. For example, when comparing dry and wet simulations initialised on April 11, 2021, moisture flux differences associated with the outflow are

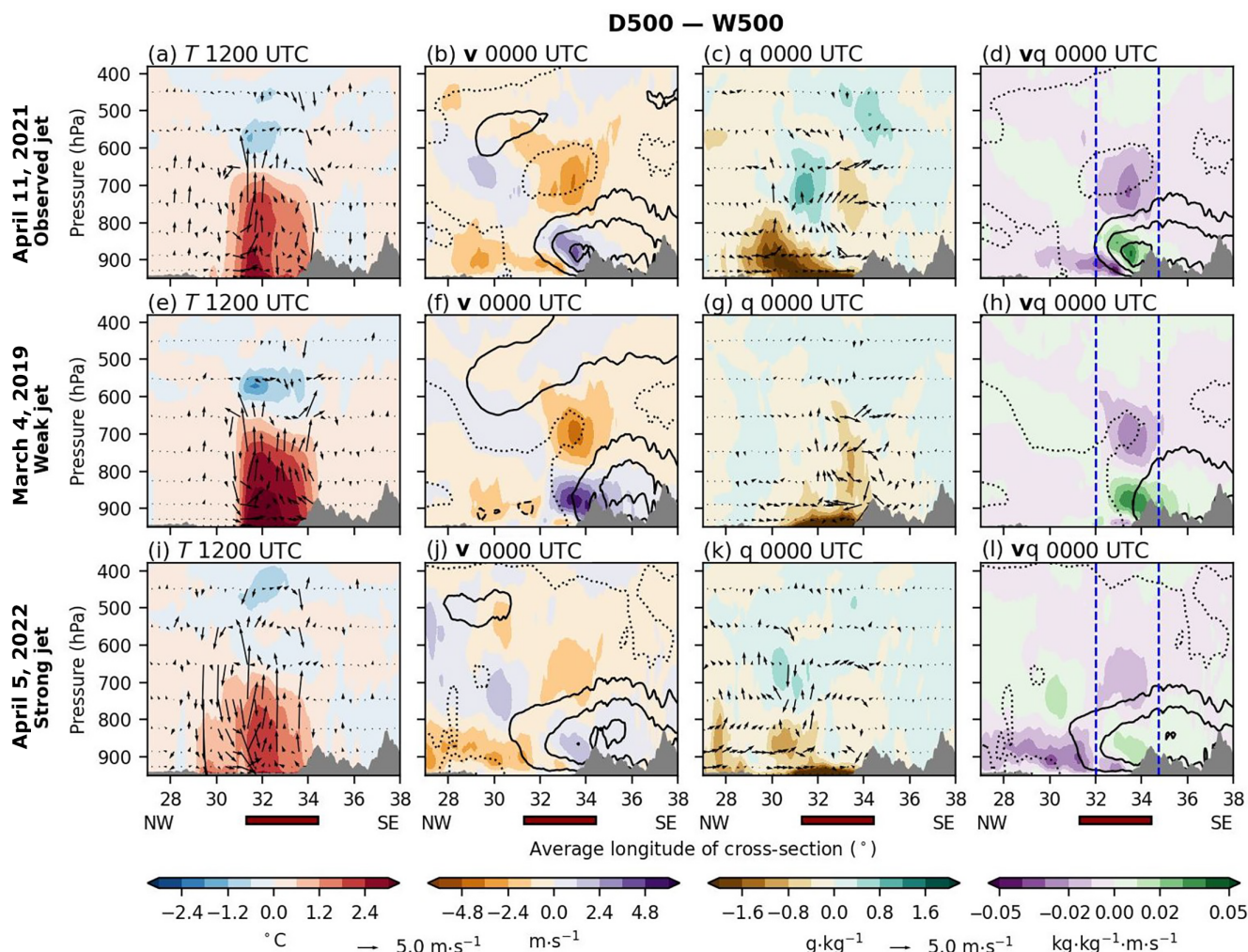


FIGURE 6 Vertical cross-sections of 10-day mean atmospheric differences between D500 and W500 simulations with prescribed soil moisture within 500 km of the Turkana channel's exit: (a, e, i) air temperature (filled, $^{\circ}\text{C}$), (b, f, j) channel-orientated wind speed (filled, $\text{m}\cdot\text{s}^{-1}$), (c, g, k) specific humidity (filled, $\text{g}\cdot\text{kg}^{-1}$), and (d, h, l) channel-orientated moisture flux (filled, $\text{kg}\cdot\text{kg}^{-1}\cdot\text{m}\cdot\text{s}^{-1}$). Arrows in the first and third columns are horizontally and (c, g, k) vertically scaled by differences in channel-orientated and vertical wind speed ($\text{m}\cdot\text{s}^{-1}$) respectively. To improve visualisation, arrows are only shown for every eighth grid point horizontally ($\approx 0.32^{\circ}$) and fifth grid point vertically. Additionally, vertical wind speeds are multiplied by 100.0. The lined contours in the second and fourth columns show absolute values from control simulations in intervals of $5\text{ m}\cdot\text{s}^{-1}$ and $0.5\text{ kg}\cdot\text{kg}^{-1}\cdot\text{m}\cdot\text{s}^{-1}$ respectively. Solid lines denote positive values, whereas dotted lines indicate the zeroth contour. Grey shading indicates the orographic cross-section, which is based on the minimum 20th percentile of simulated surface pressure between D500 and W500 across the cross-section throughout the 10-day simulation. The red rectangles below all bottom-row panels denote locations where at least one grid point has fully prescribed soil moisture. Blue dashed lines in panels (d), (h), and (l) highlight the area used to compute moisture flux profiles (Figure 7). [Colour figure can be viewed at [wileyonlinelibrary.com](https://onlinelibrary.wiley.com/doi/10.1002/qj.4972)]

approximately 60% stronger than inflow differences are (Figure 7a). The deeper extent of midlevel outflow differences compared with low-tropospheric variations weakens moisture transport from coastal East Africa to continental Africa. This highlights a mechanism with which soil moisture dampens the efficiency of the Turkana jet to advect moisture through the channel. However, model errors, such as overestimated moisture fluxes between 800 and 700 hPa due to an overestimated jet depth and a positive humidity bias (Figure 4; Warner *et al.*, 2024), must be considered. We suggest that if the Turkana jet was

constrained closer to the surface, possibly due to a shallower boundary layer and a better representation of elevated nocturnal inversions, a stronger response in low-level moisture transport could emerge, further impacting the regional-scale moisture budget. Improved jet simulations could also reduce midlevel moisture flux changes, yielding a more accurate understanding of surface–circulation interactions. In summary, though our simulations highlight that the Turkana jet is sensitive to soil moisture perturbations at the channel's exit, the surface-driven overturning circulation is associated with a

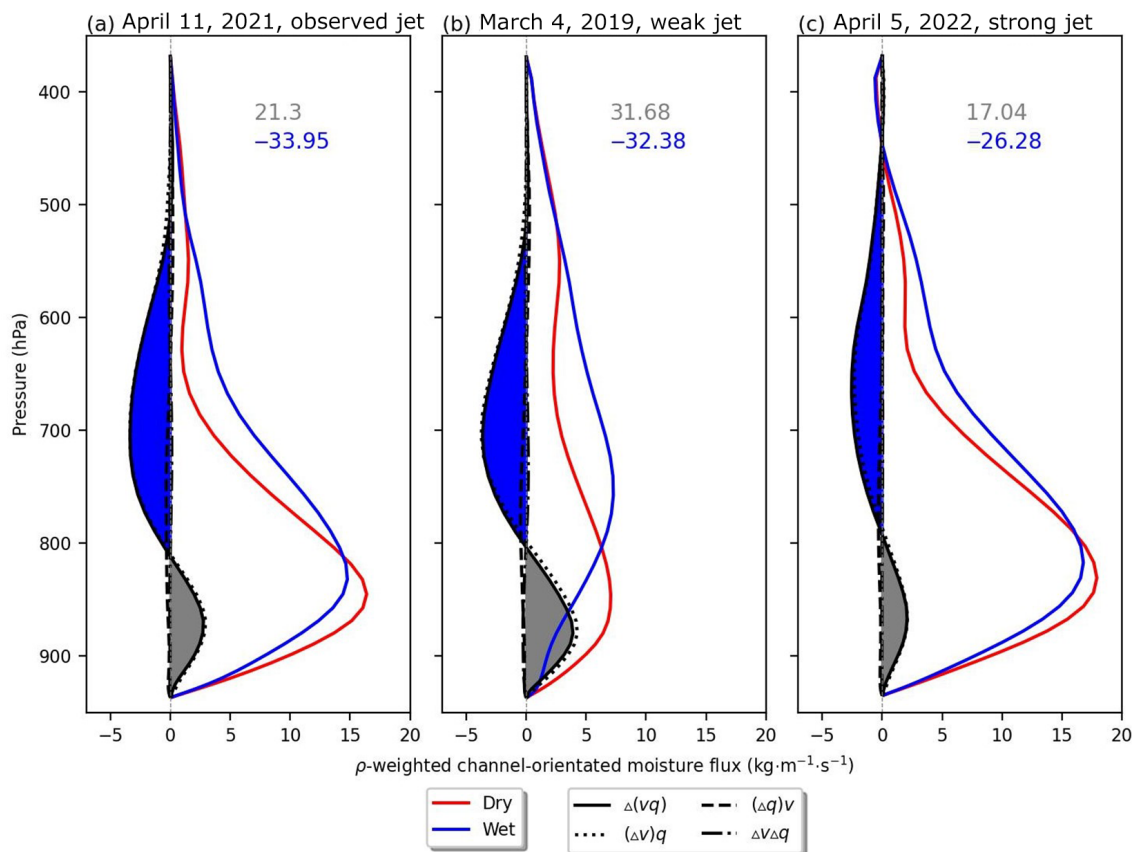


FIGURE 7 Vertical profiles of the average density-weighted channel-orientated moisture flux ($\text{kg} \cdot \text{m}^{-1} \cdot \text{s}^{-1}$) through the immediate exit of the Turkana channel (area averaged denoted by cyan rectangles in Figure 5 and cyan dashed lines in Figure 6). Red and blue lines show absolute profiles for D500 and W500 simulations respectively. Black continuous lines show the difference between D500 and W500 simulations. Grey and blue shading highlights positive and negative profile differences. The vertical integrations of positive and negative differences are labelled in the top right corner of each panel. The difference between simulations is also partitioned into changes driven by (dotted) wind, (dashed) humidity, and (dash-dotted) the product of wind and humidity differences. The profiles are shown at 0000 UTC/0300 h EAT for simulations initialised on (a) April 11, 2021, (b) March 4, 2019, and (c) April 5, 2022. [Colour figure can be viewed at wileyonlinelibrary.com]

reduced vertically integrated moisture transport between coastal East Africa and continental Africa.

So far, our analysis of the atmospheric response to fixed soil moisture perturbations has focused on 10-day averages. To illustrate sub-daily and daily variability in the jet response, Figure 8 shows temporal variations between D500 and W500 simulations in temperature, channel-orientated wind speed, and channel-orientated moisture flux at 850 hPa, as well as surface pressure and temperature at 600 hPa. The Hovmöller diagrams in Figure 8, which are centred through the Turkana channel (green rectangles in Figure 5), focus on differences between simulations commencing on March 4, 2019, with Supporting Information Figures S6 and S7 showing differences for the simulations initialised on April 11, 2021, and April 5, 2022, respectively. To the right of the Hovmöller diagrams we show the average diurnal cycle difference between dry and wet simulations, as well as tendencies

across the whole 10-day simulation. In agreement with previous studies investigating the dynamical atmospheric response to dry soils (e.g., Parker *et al.*, 2005; Rácz & Smith, 1999; Talib *et al.*, 2023), there is a diurnal variation in the thermodynamic and dynamic response to reduced soil moisture. Whereas low-level temperature differences peak at 1500 UTC/1800 h EAT (Figure 8b), due to turbulent surface fluxes and accumulated boundary-layer heat maximising at approximately midday and late afternoon respectively, wind and moisture flux differences peak at 0300 UTC/0600 h EAT (Figure 8h,k). The acceleration of low-level winds is prohibited until after sunset, as frictional forces, driven by daytime turbulent fluxes and boundary-layer turbulence, limit a low-level dynamical response during daylight hours. Finally, we also exhibit a strong diurnal cycle in atmospheric cooling at 600 hPa (Figure 8n). This midtropospheric cooling—consistent with Spengler and Smith (2008), who investigated heat

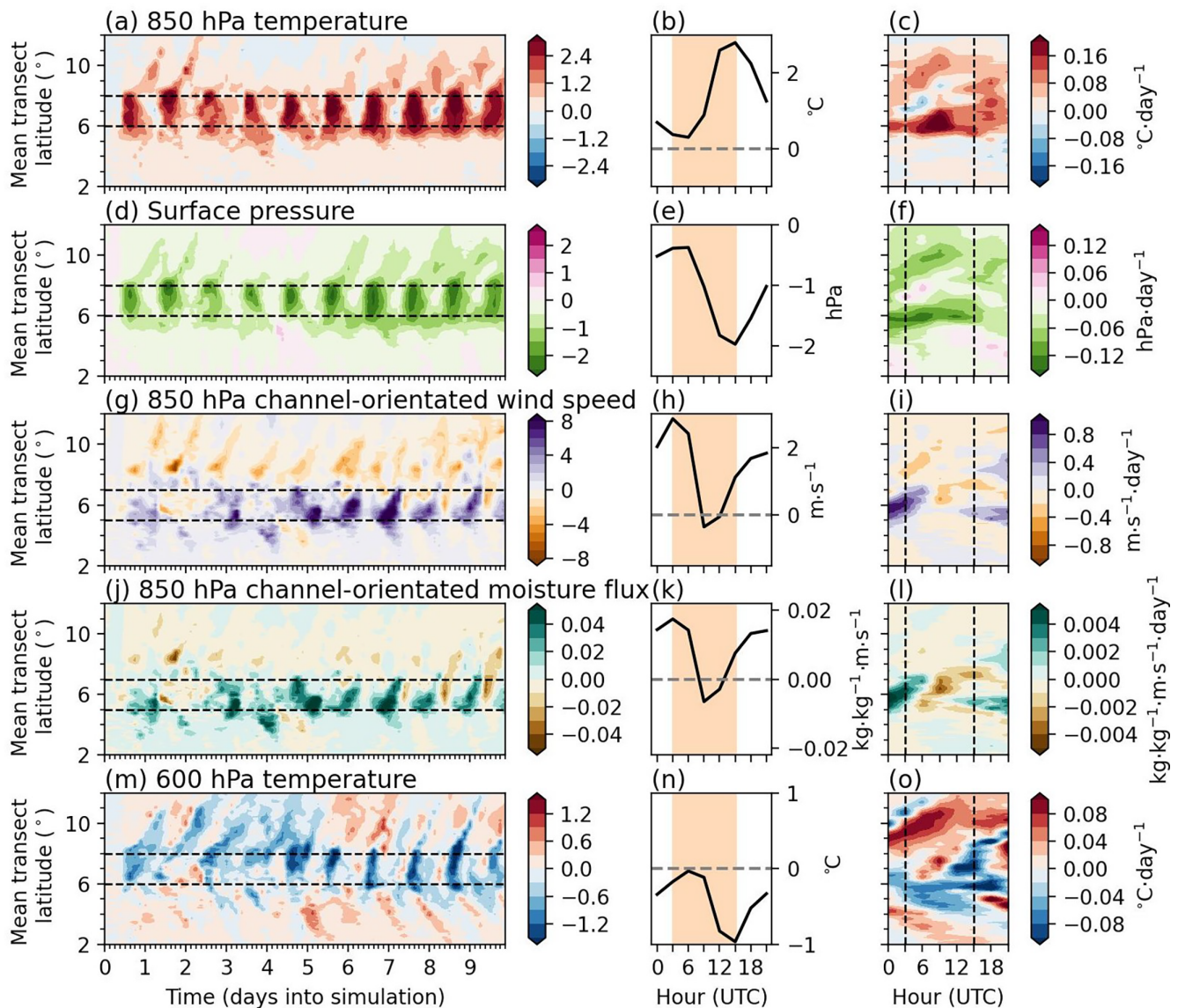


FIGURE 8 Differences between D500 and W500 simulations commencing on March 4, 2019: (a, d, g, j, m) channel-orientated Hovmöller diagrams; (b, e, h, k, n) average diurnal cycles; (c, f, i, l, o) 10-day tendencies at three-hourly intervals. The atmospheric characteristics shown are (a–c) 850 hPa temperature ($^{\circ}\text{C}$), (d–f) surface pressure (hPa), (g–i) 850 hPa channel-orientated wind speed ($\text{m} \cdot \text{s}^{-1}$), (j–l) 850 hPa channel-orientated moisture flux ($\text{kg} \cdot \text{kg}^{-1} \cdot \text{m} \cdot \text{s}^{-1}$), and (m–o) 600 hPa temperature ($^{\circ}\text{C}$). The cross-section taken for each Hovmöller diagram is orientated along the Turkana channel; shown in Figure 5). Black dashed horizontal lines in Hovmöller diagrams highlight the area used to compute differences between diurnal cycles. For temperatures and surface pressure (a–f, m–o) averages are taken between 6° N and 8° N latitude, whereas for channel-orientated diagnostics (g–l) the averages are taken between 5° N and 7° N latitude. Grey dashed horizontal lines on panels (b), (e), (h), (k), and (n) denote the zeroth value, and daytime hours (0300–1500 UTC/0600–1800 h EAT) are highlighted with a light orange background. Vertical dashed lines in panels (c), (f), (i), (l), and (o) denote sunrise (0300 UTC/0600 h EAT) and sunset (1500 UTC/1800 h EAT) hours. [Colour figure can be viewed at [wileyonlinelibrary.com](https://onlinelibrary.wiley.com/terms-and-conditions)]

low dynamics in an idealised model configuration—is associated with upper tropospheric subsidence (not shown).

In addition to illustrating diurnal variations in the atmospheric response to soil moisture perturbations, Figure 8 highlights day-to-day variability. We propose three possible mechanisms for this simulated daily variability: (1) large-scale synoptic variability controlling

the influence of soil moisture on jet characteristics; (2) cloud–radiation interactions affecting low-level heating; and (3) the impact of accumulated surface-driven heat. As proposed when considering differences between case studies, the jet sensitivity to soil moisture depends on the large-scale synoptic variability. When the along-channel pressure difference is large, and therefore large-scale circulation anomalies are the dominant

driver for jet characteristics, the influence of soil moisture on LLJ characteristics is small (Supporting Information Figure S5c). With regard to the influence of cloud–radiation interactions, Figure 8a,d indicates that the intensity of surface pressure differences depends on low-level atmospheric warming. For instance, relatively weak warming during days 2 and 3 are associated with relatively small pressure differences. Correlations between simulated midlevel cloud and atmospheric conditions illustrate that cloud–radiation interactions substantially control the amount of surface-driven atmospheric heating by reducing insolation and surface sensible heating (Supporting Information Figure S8). Reduced atmospheric warming associated with cloud–radiation interactions decreases the dynamical atmospheric response, including the acceleration of the nocturnal jet. Finally, throughout the 10-day simulation, surface-driven heating accumulates in the low-level atmosphere, especially when the Turkana jet is weak (Figure 8c). This heat accumulation gradually reduces the surface pressure in the channel's exit (Figure 8f) and intensifies nocturnal jet speeds (Figure 8i). The effect can also be seen from stronger jet differences in the latter half of the 10-day simulation compared with the former (Figure 8g). This effect of accumulated surface-driven heat on the Turkana jet is consistent with an intensification of jet anomalies during MJO events (Talib *et al.*, 2023).

3.3 | The impact of increasing the size of soil moisture perturbations

In the previous subsection we show that the Turkana jet is sensitive to soil moisture conditions in the channel's exit. However, whereas the surface-induced overturning circulation strengthens the LLJ, it reduces the total amount of moisture transported through the channel (Figure 7). Additionally, we find that simulated wind differences are constrained to within approximately 200 km of perturbed soil moisture conditions. To investigate whether these conclusions depend on the size and location of soil moisture perturbations, we perform additional atmospheric integrations with soil moisture differences that extend further away from the channel's exit or within the channel itself (Table 3).

Figure 9 shows 10-day mean differences in nocturnal channel-orientated wind speed and wind convergence at 850 hPa between all pairs of dry and wet simulations. To further support our discussion, Figure 10 shows vertical cross-sections of differences in temperature, channel-orientated wind, and channel-orientated moisture flux for simulation pairs initialised on March 4, 2019 (also shown for simulations commencing on April

11, 2021, and April 5, 2022, in Supporting Information Figures S9 and S10 respectively). For all three case studies, increasing the extent of soil moisture perturbations from 500 to 750 km (D500/W500 to D750/W750) increases the difference in nocturnal jet speeds across the channel's exit (Figure 9). For example, wind differences are approximately 50% larger when extending soil moisture perturbations to 750 km for the case study commencing on March 4, 2019 (Figures 9e and 10f and Supporting Information Figure S4b). These enhanced wind differences amplify differences in wind convergence. Interestingly, despite the 250 km extension in surface-driven anomalous heating (Figure 10b), the maximum difference in convergence and vertical wind remains fixed near 32° E (Figures 10e and 10f). This suggests that the jet is only able to extend approximately 100 km from the channel's exit, regardless of the heating extent, due to the diminishing amount of sensible heat after sunset. Furthermore, the intensified surface-induced overturning circulation when increasing the extent of soil moisture perturbations to 750 km increases the magnitude of low-tropospheric moisture transport (Figures 10i and 10j and Supporting Information Figure S11). However, we only find an enhanced jet efficiency in transporting moisture through the channel in weak jet simulations (Supporting Information Figure S11b).

On the other hand, although increasing the extent of soil moisture perturbations to 750 km intensifies surface-driven low-tropospheric heating and the associated overturning circulation, extending soil moisture perturbations by a further 250 km (D1000/W1000) leads to only minor additional atmospheric changes. Figure 10c shows that the extension of dry surface conditions to 1,000 km leads to relatively small increases in low-tropospheric temperature (approximately 1° C) between 28° E and 30° E longitude. Differences between dry and wet surface soil moisture conditions within 28° E and 30° E longitude are relatively small (Supporting Information Figure S2c), as this area is typically arid during March–May. In other words, “wet” soil moisture conditions in this region are too dry to promote substantial differences in the surface flux partitioning. Hence, additional surface heating, and the associated atmospheric response, is muted when comparing D1000 and W1000 simulations.

Finally, in addition to increasing the extent of soil moisture perturbations in the channel's exit, we also performed a set of simulations with fixed soil moisture within the channel itself (D500PC and W500PC). As concluded when only changing soil moisture conditions in the channel's exit, the atmospheric response is relatively constrained to the region of perturbed soil moisture conditions; that is, minimal wind differences are simulated in the channel's

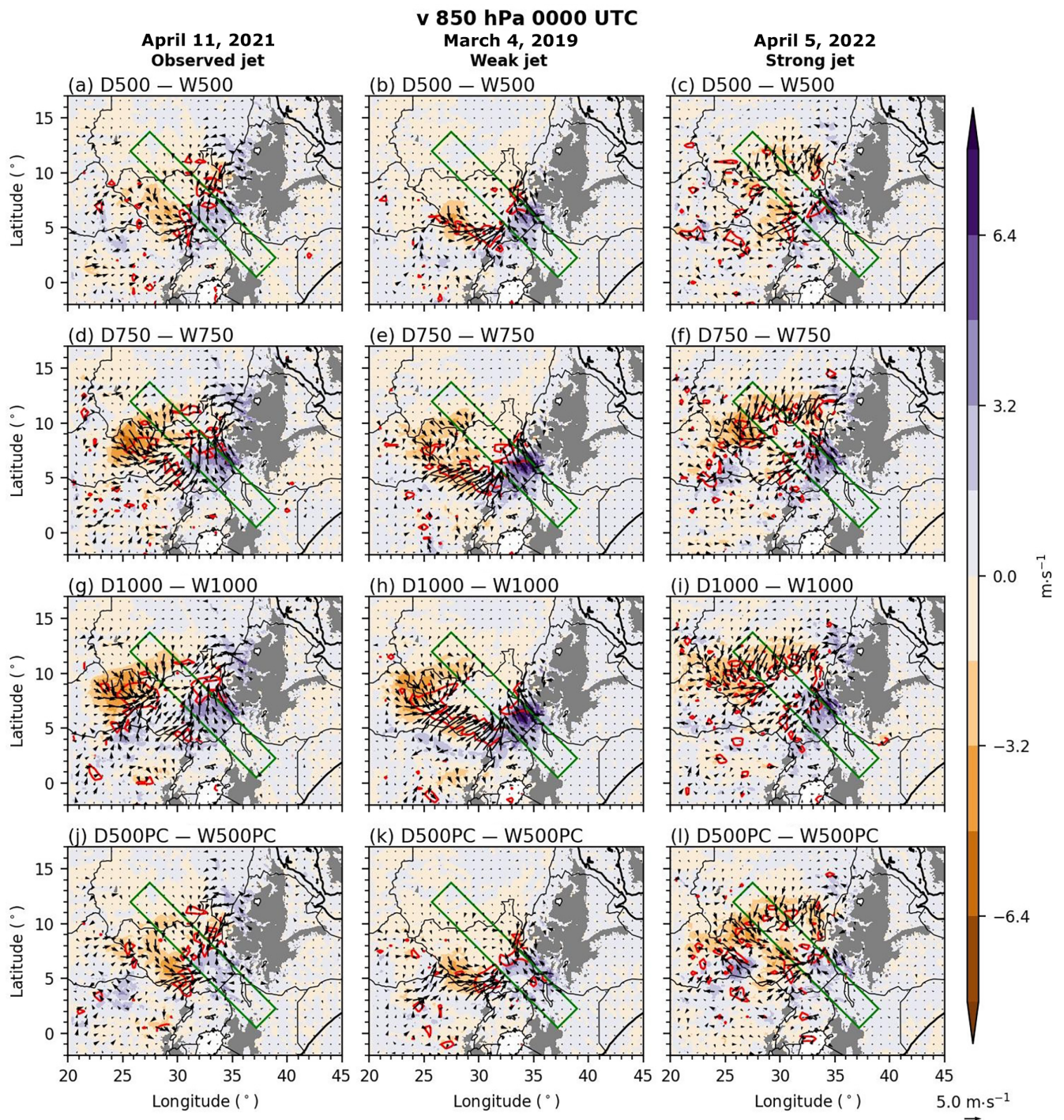


FIGURE 9 Differences in 10-day mean channel-orientated wind speed (filled, $\text{m} \cdot \text{s}^{-1}$) between dry and wet simulations. The panels show differences between (a–c) D500 and W500, (d–f) D750 and W750, (g–i) D1000 and W1000, and (j–l) D500PC and W500PC. Arrows, which are only shown for every 20th grid point ($\approx 0.8^\circ$) to improve visualisation, denote horizontal wind components. Red lined contours denote areas of wind convergence greater than $2.5 \times 10^{-5} \text{ s}^{-1}$ after downscaling to a 0.5° resolution. Left, center and right panels show simulated atmospheric differences for case studies initialised on 11th April 2021, 4th March 2019 and 5th April 2022 respectively. On all panels grey shading indicates grid points where the minimum surface pressure between the two simulations is smaller than 850 hPa at any time in the 10-day simulation. Green rectangles in all panels highlight the area used for vertical cross-sections through the Turkana channel (Figure 10 and Supporting Information Figures S9 and S10). [Colour figure can be viewed at [wileyonlinelibrary.com](https://onlinelibrary.wiley.com)]

March 4, 2019
Weak jet

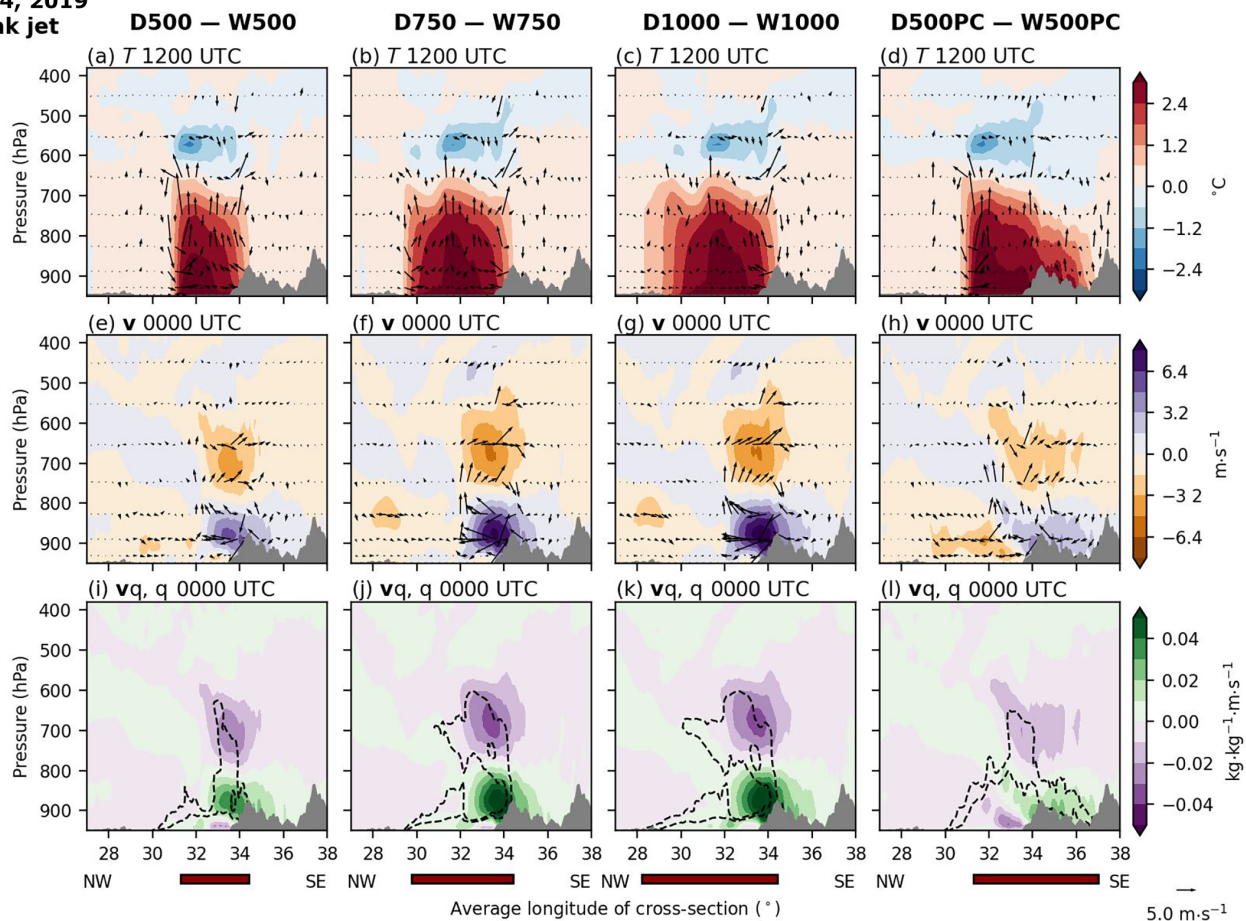


FIGURE 10 Vertical cross-sections of 10-day mean atmospheric differences between dry and wet simulations initialised on March 4, 2019. The panels show differences between (a, e, i) D500 and W500, (b, f, j) D750 and W750, (c, g, k) D1000 and W1000, and (d, h, l) D500PC and W500PC. Shown are differences in (a–d) air temperature (filled, $^{\circ}\text{C}$), (e–h) channel-orientated wind speed (filled, $\text{m} \cdot \text{s}^{-1}$), and (i–l) channel-orientated moisture flux (filled, $\text{kg} \cdot \text{kg}^{-1} \cdot \text{m} \cdot \text{s}^{-1}$). Arrows in (a)–(d) and (e)–(h) are horizontally and vertically scaled by differences in channel-orientated and vertical wind speed ($\text{m} \cdot \text{s}^{-1}$) respectively. To improve visualisation, arrows are only shown for every eighth grid point horizontally ($\approx 0.32^{\circ}$) and fifth grid point vertically. Additionally, vertical wind speeds are multiplied by 100.0. Dashed contours in (i)–(l) show differences in specific humidity at intervals of $-0.5 \text{ g} \cdot \text{kg}^{-1}$. Grey shading indicates the orographic cross-section, which is based on the minimum 20th percentile of simulated surface pressure between the two simulations across the cross-section throughout the 10-day simulation. The red rectangles below bottom-row panels denote locations where at least one grid point has fully prescribed soil moisture for each simulation set. [Colour figure can be viewed at wileyonlinelibrary.com]

entrance (Figure 9j–l). Figure 10d,h,l shows that though changing soil moisture conditions within the channel extends the region of anomalous low-tropospheric heating, the surface-driven overturning circulation is significantly weaker. As a result of this, we hypothesise that the Turkana jet is most sensitive to the temperature gradient across the channel’s exit. Hence, when extending prescribed soil moisture conditions into the channel itself, we weaken the temperature gradient across the channel’s exit and simulate a weaker jet response. Although we simulate a wind response within the channel itself, most likely due to a surface-induced pressure gradient between the entrance and centre of the channel, the wind response is relatively small due to arid conditions (Supporting

Information Figure S2c) and weak low-level temperature differences (Figure 10d) within the channel.

To summarise, in our convection-permitting model configuration, the jet response to soil moisture perturbations maximises when varying surface conditions within 750 km of the channel’s exit. Extending soil moisture perturbations further or within the channel itself does not favour a strengthened jet response due to either minimal soil moisture variability or a weakening of the surface-induced pressure gradient across the channel’s exit. Nevertheless, our simulations highlight that Turkana jet speeds can vary by up to $8 \text{ m} \cdot \text{s}^{-1}$ when realistically changing soil moisture conditions across the channel’s exit.

4 | DISCUSSION

Motivated by recent findings that soil-moisture-atmosphere feedbacks amplify MJO-induced anomalies of the Turkana jet (Talib *et al.*, 2023), this study isolates the specific influence of soil moisture on jet characteristics using convection-permitting modelling experiments. By examining simulated atmospheric differences between experiments with realistic dry or wet surface conditions across the channel's exit, we find that dry soils enhance a surface-induced thermal low, increase the along-channel pressure gradient, and intensify the nocturnal jet. Notably, under weak jet conditions, wind speeds are up to $8 \text{ m} \cdot \text{s}^{-1}$ stronger in atmospheric simulations with dry soils compared with those with wet soils. However, jet sensitivity to soil moisture is reduced when large-scale circulation patterns strongly control jet dynamics or when cloud-radiation interactions are substantial.

A major limitation of using atmospheric simulations to isolate drivers of jet variability is that most models struggle to capture characteristics of the Turkana jet (Oscar *et al.*, 2022). Though increasing model resolution to convection-permitting scales improves simulated jet speeds, even such high-resolution models have difficulty accurately resolving elevated nocturnal inversions (Figure 4; Warner *et al.*, 2024), primarily due to challenges associated with parametrisation schemes depicting processes within stable atmospheric boundary layers (Holtzlag *et al.*, 2013). In light of observations indicating that elevated inversions suppress upward momentum mixing and lead to an intensified Turkana jet (Munday *et al.*, 2024), we hypothesise that the poor representation of elevated nocturnal inversions in our simulations leads to an overestimated jet depth and a positive midtropospheric nocturnal humidity bias. Consequently, we speculate that the jet's sensitivity to soil moisture depends on the parametrisation of boundary-layer processes, with a more pronounced response expected when elevated inversions are better resolved. Future work should investigate surface-driven jet modulation using a model configuration with a boundary-layer parametrisation scheme that provides a more accurate representation of the LLJ. Furthermore, we found that surface-driven low-level moisture transport changes are counteracted by midtropospheric variations associated with the return flow of the thermally induced overturning circulation. As a result, our simulations provide limited evidence that surface-driven jet variations significantly affect continental-scale moisture budgets. A better representation of elevated inversions may reduce the sensitivity of midtropospheric moisture transport, thereby potentially increasing the sensitivity

of the vertically integrated moisture transport to surface-driven jet variations.

Additionally, it is important to acknowledge our reliance on a single atmospheric dynamical model to investigate surface-jet dynamics. Since general circulation models vary in their simulation of land-surface dynamics (Gallego-Elvira *et al.*, 2019; Mwanthi *et al.*, 2023) and soil moisture coupling with temperature and precipitation (Gevaert *et al.*, 2018; Hohenegger *et al.*, 2009; Koster *et al.*, 2006; Müller *et al.*, 2021; Taylor *et al.*, 2013), different models may exhibit varying jet sensitivities to soil moisture. Furthermore, these model discrepancies may partly explain substantial differences in simulated jet characteristics (King *et al.*, 2021; Munday *et al.*, 2021; Oscar *et al.*, 2022). Nevertheless, even though the influence of soil moisture on the Turkana jet has only been examined in one atmospheric model configuration, we provide modelling evidence that correctly capturing jet variability requires an accurate depiction of surface-jet interactions, in addition to a detailed representation of orographic processes (Warner *et al.*, 2024).

Owing to limited computational resources, which restricted the design and number of convection-permitting simulations, our investigation focused on three 10-day periods each within a long rains season. Given the pronounced seasonal variability in jet characteristics, driven by changes in continental-scale circulation patterns (Hartman, 2018; King *et al.*, 2021; Nicholson, 2016), we anticipate that the jet's sensitivity to soil moisture varies throughout the year. Additionally, the influence of soil moisture on jet characteristics is likely to vary seasonally due to differences in surface characteristics across the channel's exit (Agutu *et al.*, 2021; Rebelo *et al.*, 2012). To simplify our analysis of surface-jet interactions further, we focused on periods of rainfall deficiency, as the location of simulated deep convection varies substantially across convection-permitting experiments (Cafaro *et al.*, 2021). Simulated variations in deep convection would have made it challenging to distinguish jet variations that are solely driven by prescribed soil moisture variations and not due to differences in convection. Consistent with a reduced soil-moisture-jet coupling under increased midlevel cloud cover (Supporting Information Figure S8), we hypothesise that reduced surface insolation during periods of deep convection dampens both the surface flux and atmospheric response to soil moisture variations. Moreover, enhanced deep convection may modify low-level convergence patterns near the periphery of the Turkana channel, further influencing jet sensitivity. To fully understand the jet's response to soil moisture in a highly convective environment requires a large ensemble of simulations that capture the range of jet responses in different convective

conditions. Considering the jet is most sensitive to soil moisture variations under clear skies, the jet may be particularly responsive to surface variations outside the local rainy seasons.

Given the relatively low forecast skill across East Africa (Cafaro *et al.*, 2021; de Andrade *et al.*, 2021; Gudoshava *et al.*, 2024; Mwangi *et al.*, 2014; Young & Klingaman, 2020) and the growing demand for skilful atmospheric predictions (Gudoshava *et al.*, 2022; Hirons *et al.*, 2021), there is an urgent need for reliable predictions of East African atmospheric variability. One way to enhance forecasts of the Turkana jet is through improving the representation of surface characteristics across the channel's exit. This is particularly challenging, as much of South Sudan is a floodplain (Marthews *et al.*, 2022; Parker *et al.*, 2022), where, after heavy rainfall, upstream flows can saturate wetlands for several months (Basheer *et al.*, 2023; Mohamed & Savenije, 2014; Sutcliffe & Brown, 2018). Such surface saturation can dramatically alter the partitioning of surface fluxes, which in turn influences the Turkana jet. Current numerical weather prediction models do not simulate crucial fluvial inundation processes, thereby missing this important source of surface-driven predictability. Though the assimilation of satellite-derived observations has improved the initialisation of soil moisture in operational predictions (De Rosnay *et al.*, 2013; Draper & Reichle, 2019; Gómez *et al.*, 2020), the evolution of soil moisture throughout the forecast is poorly represented and affects the representation of soil-moisture-atmosphere coupling (Dirmeyer *et al.*, 2018). For example, in line with Gallego-Elvira *et al.* (2019), our simulations show that surface evaporation is overestimated in wet, energy-limited regions (not shown). In the context of the Turkana jet, simulated wet soils in the channel's exit, which weaken the jet, are unlikely to persist beyond several days due to rapid surface drying. We further hypothesise that improving the accuracy of Turkana jet predictions could lead to better forecasts of other key components of the African climate system. For instance, moisture transport through the Turkana channel plays an important role in the formation and development of African easterly waves to the west of the Ethiopian Highlands (Hamilton *et al.*, 2020; Núñez Ocasio *et al.*, 2021; White *et al.*, 2021). These African easterly waves propagate along the African easterly jet (Mathon *et al.*, 2002b) and partly control the location of Sahelian mesoscale convection systems (Janiga & Thorncroft, 2016; Mathon *et al.*, 2002a; Núñez Ocasio *et al.*, 2021).

This study contributes to the growing body of research that examines regional-scale atmospheric dynamical changes in response to anomalous surface conditions (Bieri *et al.*, 2021; Chen & Dominguez, 2024; Correa *et al.*, 2024; Matus *et al.*, 2023; Talib *et al.*, 2021, 2022).

Although previous modelling efforts have demonstrated that improving soil moisture initialisation enhances subseasonal forecast skill for temperature and, to a lesser extent, precipitation (Dirmeyer *et al.*, 2018; Gómez *et al.*, 2020; Koster *et al.*, 2006, 2011), these studies have primarily focused on localised surface-atmosphere interactions. In light of a growing demand for skilful atmospheric predictions, there is a continued need to quantify surface-driven dynamical predictability and its impact on local weather. The Turkana jet, situated across a steep aridity gradient, is a hotspot for surface-jet interactions. In light of observations that suggest surface changes across this aridity gradient influence MJO-induced jet anomalies (Talib *et al.*, 2023), there is an opportunity to quantify surface-driven subseasonal predictability of jet anomalies. Furthermore, most research, including this study, focuses on surface-driven dynamical changes in specific regions. Expanding this work, there is a clear opportunity to develop a global framework that quantifies dynamical atmospheric responses to surface variability, and to evaluate such processes in forecast and climate models.

5 | CONCLUSIONS

By analysing MetUM convection-permitting simulations with prescribed soil moisture conditions, we highlight that surface characteristics at the Turkana channel's exit can substantially influence the strength of the nocturnal jet. Simulated jet speed differences peak at approximately $8 \text{ m} \cdot \text{s}^{-1}$ when comparing atmospheric integrations with fixed dry or wet surface conditions across the lowlands of South Sudan. Drier soils in the channel's exit enhance surface warming, promote a local surface-induced thermal low circulation, intensify the along-channel pressure gradient, and strengthen the LLJ. However, jet sensitivity to soil moisture reduces when the synoptic-scale circulation substantially controls jet characteristics or when cloud-radiation interactions reduce surface insolation. Additionally, despite jet intensification when prescribing dry soils, there is no significant increase in the vertically integrated moisture transport through the channel, nor does it notably impact continental-scale moisture budgets. This is because the return flow associated with the thermally induced circulation transports similar moisture amounts to that exhibited at low levels. However, we speculate that midtropospheric moisture transports are too large due to a positive midlevel humidity bias. This study is the first to use modelling experiments to show that soil moisture may be a source of predictability for forecasting characteristics of the Turkana jet. Future experiments should focus on fully isolating the predictive skill that can

be derived from land-surface processes in this sensitive region.

AUTHOR CONTRIBUTIONS

Joshua Talib: conceptualization; investigation; funding acquisition; writing – original draft; methodology; validation; visualization; writing – review and editing; software; formal analysis; project administration; data curation; supervision; resources. **Christopher M. Taylor:** conceptualization; funding acquisition; writing – review and editing; methodology; project administration; supervision. **Cornelia Klein:** conceptualization; funding acquisition; writing – review and editing; methodology; project administration; supervision. **James Warner:** data curation; writing – review and editing; methodology; resources. **Callum Munday:** data curation; resources; writing – review and editing; methodology. **Sonja Folwell:** writing – review and editing; conceptualization. **Cristina Charlton-Perez:** writing – review and editing; conceptualization; methodology; software.

ACKNOWLEDGEMENTS

This work and several contributors (JT, CT, CK, SF) were supported by the Natural Environment Research Council (NERC) as part of the NC-international programme (NE/X006247/1) delivering National Capability. CK acknowledges funding from the NERC independent research fellowship, Continental convective organisation and rainfall intensification in a warming world: improving storm predictions from hours to decades (COCOON; NE/X017419/1). This work and its contributors (James Warner) were funded by the Met Office Weather and Climate Science for Service Partnership (WCSSP) South Africa project, which is supported by the Department for Science, Innovation & Technology (DSIT). The RIFTJet project, as well as support for CM, are part of the REACH (programme code 201880) water security programme funded by the Foreign, Commonwealth & Development Office (FCDO). The RIFTJet project included partnerships with the Kenya Meteorological Department and University of Nairobi. However, the views expressed, and information contained in it, are not necessarily those of or endorsed by the FCDO, which can accept no responsibility for such views or information or for any reliance placed on them.

We would like to thank the anonymous reviewers for their constructive comments. Additionally, thanks to Dr Fran Morris (University of Oxford), Dr Helen Burns (Centre for Environmental Modelling And Computation, University of Leeds), and those at the National Centre for Atmospheric Science Computational Modelling Services (NCAS-CMS) for their discussions whilst developing model sensitivity experiments. We would also like

to acknowledge the Hydro-JULES Research Exchange Programme (grant number NE/X019063/1) for enabling collaborative discussions between JT and CCP.

DATA AVAILABILITY STATEMENT

All observational data used in this study are freely available. ESA CCI soil moisture satellite observations and CHIRPS precipitation were accessed at www.esa-soilmoisture-cci.org and <https://www.chc.ucsb.edu/data/chirps> respectively. ERA5 data were accessed at <https://cds.climate.copernicus.eu/cdsapp/home>.

ORCID

Joshua Talib  <https://orcid.org/0000-0002-4183-1973>

Christopher M. Taylor  <https://orcid.org/0000-0002-0120-3198>

-0120-3198

Cornelia Klein  <https://orcid.org/0000-0001-6686-0458>

James Warner  <https://orcid.org/0000-0002-9318-8385>

Callum Munday  <https://orcid.org/0000-0002-6436-5813>

-5813

Sonja Folwell  <https://orcid.org/0000-0001-5745-4116>

Cristina Charlton-Perez  <https://orcid.org/0000-0002-7805-5955>

-7805-5955

REFERENCES

- Agutu, N., Ndehedehe, C., Awange, J., Kirimi, F. & Mwaniki, M. (2021) Understanding uncertainty of model-reanalysis soil moisture within greater horn of Africa (1982–2014). *Journal of Hydrology*, 603, 127169.
- de Andrade, F.M., Young, M.P., MacLeod, D., Hirons, L.C., Woolnough, S.J. & Black, E. (2021) Subseasonal precipitation prediction for Africa: forecast evaluation and sources of predictability. *Weather Forecasting*, 36, 265–284.
- Basheer, M., Nechifor, V., Calzadilla, A., Gebrechorkos, S., Pritchard, D., Forsythe, N. et al. (2023) Cooperative adaptive management of the Nile River with climate and socio-economic uncertainties. *Nature Climate Change*, 13, 48–57.
- Berg, A., Lintner, B.R., Findell, K.L., Malyshev, S., Loikith, P.C. & Gentine, P. (2014) Impact of soil moisture–atmosphere interactions on surface temperature distribution. *Journal of Climate*, 27, 7976–7993.
- Berg, L.K., Riihimaki, L.D., Qian, Y., Yan, H. & Huang, M. (2015) The low-level jet over the southern Great Plains determined from observations and reanalyses and its impact on moisture transport. *Journal of Climate*, 28, 6682–6706.
- Berg, A., Lintner, B., Findell, K. & Giannini, A. (2017) Soil moisture influence on seasonality and large-scale circulation in simulations of the west African monsoon. *Journal of Climate*, 30, 2295–2317.
- Berhane, F. & Zaitchik, B. (2014) Modulation of daily precipitation over East Africa by the Madden–Julian oscillation. *Journal of Climate*, 27, 6016–6034.
- Best, M.J., Pryor, M., Clark, D., Rooney, G.G., Essery, R., Ménard, C. et al. (2011) The joint UK land environment simulator (JULES), model description–part 1: energy and water fluxes. *Geoscientific Model Development*, 4, 677–699.

- Bieri, C.A., Dominguez, F. & Lawrence, D.M. (2021) Impacts of large-scale soil moisture anomalies on the hydroclimate of southeastern South America. *Journal of Hydrometeorology*, 22, 657–669.
- Burrows, D.A., Ferguson, C.R., Campbell, M.A., Xia, G. & Bosart, L.F. (2019) An objective classification and analysis of upper-level coupling to the Great Plains low-level jet over the twentieth century. *Journal of Climate*, 32, 7127–7152.
- Bush, M., Allen, T., Bain, C., Boutle, I., Edwards, J., Finnenkoetter, A. et al. (2020) The first met Office unified model–JULES regional atmosphere and land configuration, RAL1. *Geoscientific Model Development*, 13, 1999–2029.
- Bush, M., Boutle, I., Edwards, J., Finnenkoetter, A., Franklin, C., Hanley, K. et al. (2023) The second met Office unified model–JULES regional atmosphere and land configuration, RAL2. *Geoscientific Model Development*, 16, 1713–1734.
- Cafaro, C., Woodhams, B.J., Stein, T.H., Birch, C.E., Webster, S., Bain, C.L. et al. (2021) Do convection-permitting ensembles lead to more skillful short-range probabilistic rainfall forecasts over tropical East Africa? *Weather and Forecasting*, 36, 697–716.
- Campbell, M.A., Ferguson, C.R., Burrows, D.A., Beauharnois, M., Xia, G. & Bosart, L.F. (2019) Diurnal effects of regional soil moisture anomalies on the Great Plains low-level jet. *Monthly Weather Review*, 147, 4611–4631.
- Chen, C.-C. & Dominguez, F. (2024) The location of large-scale soil moisture anomalies affects moisture transport and precipitation over southeastern South America. *Geophysical Research Letters*, 51, e2023GL106777.
- Chen, R. & Tomassini, L. (2015) The role of moisture in summertime low-level jet formation and associated rainfall over the east Asian monsoon region. *Journal of the Atmospheric Sciences*, 72, 3871–3890.
- Chug, D. & Dominguez, F. (2019) Isolating the observed influence of vegetation variability on the climate of La Plata river basin. *Journal of Climate*, 32, 4473–4490.
- Cioni, G. & Hohenegger, C. (2017) Effect of soil moisture on diurnal convection and precipitation in large-eddy simulations. *Journal of Hydrometeorology*, 18, 1885–1903.
- Clark, D., Mercado, L., Sitch, S., Jones, C., Gedney, N., Best, M. et al. (2011) The joint UK land environment simulator (JULES), model description–part 2: carbon fluxes and vegetation dynamics. *Geoscientific Model Development*, 4, 701–722.
- Copernicus Climate Change Service (C3S) (2017) ERA5: fifth generation of ECMWF atmospheric reanalyses of the global climate. *Copernicus Climate Change Service Climate Data Store (CDS)*. Available from: URL: <https://cds.climate.copernicus.eu/cdsapp!/home>.
- Correa, I.C., Arias, P.A., Vieira, S.C. & Martínez, J.A. (2024) A drier Orinoco basin during the twenty-first century: the role of the Orinoco low-level jet. *Climate Dynamics*, 62, 2369–2398.
- De Rosnay, P., Drusch, M., Vasiljevic, D., Balsamo, G., Albergel, C. & Isaksen, L. (2013) A simplified extended Kalman filter for the global operational soil moisture analysis at ECMWF. *Quarterly Journal of the Royal Meteorological Society*, 139, 1199–1213.
- Dharssi, I., Bovis, K., Macpherson, B. & Jones, C.P. (2011) Operational assimilation of ASCAT surface soil wetness at the met Office. *Hydrology and Earth System Sciences*, 15, 2729–2746.
- Dirmeyer, P.A., Halder, S. & Bombardi, R. (2018) On the harvest of predictability from land states in a global forecast model. *Journal of Geophysical Research: Atmospheres*, 123, 13–111.
- Dorigo, W., Wagner, W., Albergel, C., Albrecht, F., Balsamo, G., Brocca, L. et al. (2017) ESA CCI soil moisture for improved earth system understanding: state-of-the art and future directions. *Remote Sensing of Environment*, 203, 185–215.
- Draper, C. & Reichle, R.H. (2019) Assimilation of satellite soil moisture for improved atmospheric reanalyses. *Monthly Weather Review*, 147, 2163–2188.
- Ferguson, C.R., Agrawal, S., Beauharnois, M.C., Xia, G., Burrows, D.A. & Bosart, L.F. (2020) Assimilation of satellite-derived soil moisture for improved forecasts of the great plains low-level jet. *Monthly Weather Review*, 148, 4607–4627.
- Findlater, J. (1969) A major low-level air current near the Indian Ocean during the northern summer. *Quarterly Journal of the Royal Meteorological Society*, 95, 362–380.
- Fletcher, J., Diop, C., Adefisan, E., Ahiataku, M., Ansah, S., Birch, C. et al. (2022) Tropical Africa's first testbed for high-impact weather forecasting and nowcasting. *Bulletin of the American Meteorological Society*, 104(8), E1409–E1425.
- Funk, C., Peterson, P., Landsfeld, M., Pedreros, D., Verdin, J., Shukla, S. et al. (2015) The climate hazards infrared precipitation with stations—a new environmental record for monitoring extremes. *Scientific Data*, 2, 1–21.
- Funk, C., Fink, A.H., Harrison, L., Segele, Z., Endris, H.S., Galu, G. et al. (2023) Frequent but predictable droughts in East Africa driven by a Walker circulation intensification. *Earth's Future*, 11, e2022EF003454.
- Gaertner, M., Dominguez, M. & Garvert, M. (2010) A modelling case-study of soil moisture–atmosphere coupling. *Quarterly Journal of the Royal Meteorological Society*, 136, 483–495.
- Gallego-Elvira, B., Taylor, C.M., Harris, P.P., Ghent, D., Veal, K.L. & Folwell, S.S. (2016) Global observational diagnosis of soil moisture control on the land surface energy balance. *Geophysical Research Letters*, 43, 2623–2631.
- Gallego-Elvira, B., Taylor, C.M., Harris, P.P. & Ghent, D. (2019) Evaluation of regional-scale soil moisture-surface flux dynamics in earth system models based on satellite observations of land surface temperature. *Geophysical Research Letters*, 46, 5480–5488.
- Gevaert, A., Miralles, D.G., de Jeu, R.A., Schellekens, J. & Dolman, A.J. (2018) Soil moisture-temperature coupling in a set of land surface models. *Journal of Geophysical Research: Atmospheres*, 123, 1481–1498.
- Gómez, B., Charlton-Pérez, C.L., Lewis, H. & Candy, B. (2020) The met Office operational soil moisture analysis system. *Remote Sensing*, 12, 3691.
- Grimm, A.M., Pal, J.S. & Giorgi, F. (2007) Connection between spring conditions and peak summer monsoon rainfall in South America: role of soil moisture, surface temperature, and topography in eastern Brazil. *Journal of Climate*, 20, 5929–5945.
- Gruber, A., Dorigo, W.A., Crow, W. & Wagner, W. (2017) Triple collocation-based merging of satellite soil moisture retrievals. *IEEE Transactions on Geoscience and Remote Sensing*, 55, 6780–6792.
- Gruber, A., Scanlon, T., van der Schalie, R., Wagner, W. & Dorigo, W. (2019) Evolution of the ESA CCI soil moisture climate data records and their underlying merging methodology. *Earth System Science Data*, 11, 717–739.

- Gudoshava, M., Wanzala, M., Thompson, E., Mwesigwa, J., Endris, H.S., Segele, Z. et al. (2022) Application of real time S2S forecasts over eastern Africa in the co-production of climate services. *Climate Services*, 27, 100319.
- Gudoshava, M., Nyinguro, P., Talib, J., Wainwright, C., Mwanthi, A., Hirons, L. et al. (2024) Drivers of sub-seasonal extreme rainfall and their representation in ECMWF forecasts during the eastern African march-to-may seasons of 2018 to 2020. *Meteorological Applications*, 31(5), e70000.
- Hamilton, H., Núñez Ocasio, K., Evans, J., Young, G. & Fuentes, J. (2020) Topographic influence on the African easterly jet and African easterly wave energetics. *Journal of Geophysical Research: Atmospheres*, 125, e2019JD032138.
- Hartman, A.T. (2018) An analysis of the effects of temperatures and circulations on the strength of the low-level jet in the Turkana Channel in East Africa. *Theoretical and Applied Climatology*, 132, 1003–1017.
- Hersbach, H., de Rosnay, P., Bell, B., Schepers, D., Simmons, A., Soci, C. et al. (2018) Operational global reanalysis: Progress, future directions and synergies with NWP. URL <https://www.ecmwf.int/node/18765>
- Hersbach, H., Bell, W., Berrisford, P., Horányi, A., Mñoz-Sabater, J., Nicolas, J., Radu, R., Schepers, D., Simmons, A., Soci, C. and Dee, D. (2019) Global reanalysis: Goodbye ERA-Interim, hello ERA5. 17–24. URL: <https://www.ecmwf.int/node/19027>.
- Hersbach, H., Bell, B., Berrisford, P., Hirahara, S., Horányi, A., Muñoz-Sabater, J. et al. (2020) The ERA5 global reanalysis. *Quarterly Journal of the Royal Meteorological Society*, 146, 1999–2049.
- Hirons, L., Thompson, E., Dione, C., Indasi, V.S., Kilavi, M., Nkiaka, E. et al. (2021) Using co-production to improve the appropriate use of sub-seasonal forecasts in Africa. *Climate Services*, 23, 100246.
- Hohenegger, C., Brockhaus, P., Bretherton, C.S. & Schär, C. (2009) The soil moisture–precipitation feedback in simulations with explicit and parameterized convection. *Journal of Climate*, 22, 5003–5020.
- Holton, J.R. (1967) The diurnal boundary layer wind oscillation above sloping terrain. *Tellus*, 19, 200–205.
- Holtzlag, A., Svensson, G., Baas, P., Basu, S., Beare, B., Beljaars, A. et al. (2013) Stable atmospheric boundary layers and diurnal cycles: challenges for weather and climate models. *Bulletin of the American Meteorological Society*, 94, 1691–1706.
- Howard, E. & Washington, R. (2018) Characterizing the synoptic expression of the Angola low. *Journal of Climate*, 31, 7147–7165.
- Indeje, M., Semazzi, F.H., Xie, L. & Ogallo, L.J. (2001) Mechanistic model simulations of the east African climate using NCAR regional climate model: influence of large-scale orography on the Turkana low-level jet. *Journal of Climate*, 14, 2710–2724.
- Janiga, M.A. & Thorncroft, C.D. (2016) The influence of African easterly waves on convection over tropical Africa and the east Atlantic. *Monthly Weather Review*, 144, 171–192.
- Kilavi, M., MacLeod, D., Ambani, M., Robbins, J., Dankers, R., Graham, R. et al. (2018) Extreme rainfall and flooding over central Kenya including Nairobi city during the long-rains season 2018: causes, predictability, and potential for early warning and actions. *Atmosphere*, 9, 472.
- King, J.A., Engelstaedter, S., Washington, R. & Munday, C. (2021) Variability of the Turkana low-level jet in reanalysis and models: implications for rainfall. *Journal of Geophysical Research: Atmospheres*, 126, e2020JD034154.
- Kinuthia, J.H. (1992) Horizontal and vertical structure of the Lake Turkana jet. *Journal of Applied Meteorology and Climatology*, 31, 1248–1274.
- Kinuthia, J. & Asnani, G. (1982) A newly found jet in North Kenya (Turkana Channel). *Monthly Weather Review*, 110, 1722–1728.
- Klein, C. & Taylor, C.M. (2020) Dry soils can intensify mesoscale convective systems. *Proceedings of the National Academy of Sciences*, 117, 21132–21137.
- Koster, R.D., Sud, Y., Guo, Z., Dirmeyer, P.A., Bonan, G., Oleson, K.W. et al. (2006) GLACE: the global land–atmosphere coupling experiment. *Part I: Overview Journal of Hydrometeorology*, 7, 590–610.
- Koster, R., Schubert, S. & Suarez, M. (2009) Analyzing the concurrence of meteorological droughts and warm periods, with implications for the determination of evaporative regime. *Journal of Climate*, 22, 3331–3341.
- Koster, R., Mahanama, S., Yamada, T., Balsamo, G., Berg, A., Boisserie, M. et al. (2011) The second phase of the global land–atmosphere coupling experiment: soil moisture contributions to subseasonal forecast skill. *Journal of Hydrometeorology*, 12, 805–822.
- Lyon, B. (2014) Seasonal drought in the greater horn of Africa and its recent increase during the march–may long rains. *Journal of Climate*, 27, 7953–7975.
- MacLeod, D. (2018) Seasonal predictability of onset and cessation of the east African rains. *Weather and Climate Extremes*, 21, 27–35.
- Madden, R.A. & Julian, P.R. (1994) Observations of the 40–50-day tropical oscillation—a review. *Monthly Weather Review*, 122, 814–837.
- Marthews, T.R., Dadson, S.J., Clark, D.B., Blyth, E.M., Hayman, G.D., Yamazaki, D. et al. (2022) Inundation prediction in tropical wetlands from JULES-CaMa-flood global land surface simulations. *Hydrology and Earth System Sciences*, 26, 3151–3175.
- Mathon, V., Diedhiou, A. & Laurent, H. (2002a) Relationship between easterly waves and mesoscale convective systems over the Sahel. *Geophysical Research Letters*, 29, 57.
- Mathon, V., Laurent, H. & Lebel, T. (2002b) Mesoscale convective system rainfall in the Sahel. *Journal of Applied Meteorology and Climatology*, 41, 1081–1092.
- Matus, S.A., Dominguez, F. & Ford, T.W. (2023) Land and atmosphere conditions prior to extreme Great Plains low-level jets. *Journal of Hydrometeorology*, 24, 783–800.
- Miralles, D., Van Den Berg, M., Teuling, A. & De Jeu, R. (2012) Soil moisture–temperature coupling: a multiscale observational analysis. *Geophysical Research Letters*, 39, L21707.
- Mohamed, Y. & Savenije, H. (2014) Impact of climate variability on the hydrology of the Sudd wetland: signals derived from long term (1900–2000) water balance computations. *Wetlands Ecology and Management*, 22, 191–198.
- Montini, T.L., Jones, C. & Carvalho, L.M. (2019) The south American low-level jet: a new climatology, variability, and changes. *Journal of Geophysical Research: Atmospheres*, 124, 1200–1218.
- Müller, O.V., Vidale, P.L., Vannièrè, B., Schiemann, R., Senan, R., Haarsma, R.J. et al. (2021) Land–atmosphere coupling sensitivity to GCMs resolution: a multimodel assessment of local and remote processes in the Sahel hot spot. *Journal of Climate*, 34, 967–985.
- Munday, C., Washington, R. & Hart, N. (2021) African low-level jets and their importance for water vapor transport and rainfall. *Geophysical Research Letters*, 48, e2020GL090999.
- Munday, C., Engelstaedter, S., Ouma, G., Ogotu, G., Olago, D., Ong'ech, D. et al. (2022) Observations of the Turkana jet and the

- east African dry tropics: the RIFTJet field campaign. *Bulletin of the American Meteorological Society*, 103, E1828–E1842.
- Munday, C., Engelstaedter, S., Washington, R., Ogotu, G., Olago, D., Ouma, G. et al. (2023a) The Turkana jet diurnal cycle in observations and reanalysis. *Journal of Climate*, 37(18), 4633–4645.
- Munday, C., Savage, N., Jones, R.G. & Washington, R. (2023b) Valley formation aridifies East Africa and elevates Congo Basin rainfall. *Nature*, 615, 276–279.
- Munday, C., Engelstaedter, S., Washington, R., Ogotu, G., Olago, D., Ouma, G. et al. (2024) The Turkana jet diurnal cycle in observations and reanalysis. *Journal of Climate*, 37, 4633–4645.
- Mutai, C.C. & Ward, M.N. (2000) East African rainfall and the tropical circulation/convection on intraseasonal to interannual timescales. *Journal of Climate*, 13, 3915–3939.
- Mwangi, E., Wetterhall, F., Dutra, E., Di Giuseppe, F. & Pappenberger, F. (2014) Forecasting droughts in East Africa. *Hydrology and Earth System Sciences*, 18, 611–620.
- Mwanthi, A., Mutemi, J., Dyer, E., James, R., Opijah, F., Webb, T. et al. (2023) Representation of land–atmosphere coupling processes over Africa in coupled model intercomparison project phase 6. *Climate Dynamics*, 62(9), 8389–8401.
- Nicholson, S.E. (2014) The predictability of rainfall over the greater horn of Africa. Part I: prediction of seasonal rainfall. *Journal of Hydrometeorology*, 15, 1011–1027.
- Nicholson, S.E. (2016) The Turkana low-level jet: mean climatology and association with regional aridity. *International Journal of Climatology*, 36, 2598–2614.
- Nicholson, S.E. (2017) Climate and climatic variability of rainfall over eastern Africa. *Reviews of Geophysics*, 55, 590–635.
- Núñez Ocasio, K.M., Brammer, A., Evans, J.L., Young, G.S. & Moon, Z.L. (2021) Favorable monsoon environment over eastern Africa for subsequent tropical cyclogenesis of African easterly waves. *Journal of the Atmospheric Sciences*, 78, 2911–2925.
- Oscar, L., Nzau, M.J., Ellen, D., Franklin, O., Rachel, J., Richard, W. et al. (2022) Characteristics of the Turkana low-level jet stream and the associated rainfall in CMIP6 models. *Climate Dynamics*, 62(9), 8371–8387.
- Palmer, P.I., Wainwright, C.M., Dong, B., Maidment, R.I., Wheeler, K.G., Gedney, N. et al. (2023) Drivers and impacts of eastern African rainfall variability. *Nature Reviews Earth and Environment*, 4, 254–270.
- Parish, T.R. & Oolman, L.D. (2010) On the role of sloping terrain in the forcing of the Great Plains low-level jet. *Journal of the Atmospheric Sciences*, 67, 2690–2699.
- Parker, D., Burton, R., Diongue-Niang, A., Ellis, R., Felton, M., Taylor, C. et al. (2005) The diurnal cycle of the west African monsoon circulation. *Quarterly Journal of the Royal Meteorological Society*, 131, 2839–2860.
- Parker, R.J., Wilson, C., Comyn-Platt, E., Hayman, G., Marthews, T.R., Bloom, A.A. et al. (2022) Evaluation of wetland CH₄ in the joint UK land environment simulator (JULES) land surface model using satellite observations. *Biogeosciences*, 19, 5779–5805.
- Pielke, R.A., Sr. (2001) Influence of the spatial distribution of vegetation and soils on the prediction of cumulus convective rainfall. *Reviews of Geophysics*, 39, 151–177.
- Pohl, B. & Camberlin, P. (2006) Influence of the Madden–Julian oscillation on east African rainfall. I: Intraseasonal variability and regional dependency. *Quarterly Journal of the Royal Meteorological Society*, 132, 2521–2539.
- Rác, Z. & Smith, R.K. (1999) The dynamics of heat lows. *Quarterly Journal of the Royal Meteorological Society*, 125, 225–252.
- Rebello, L.-M., Senay, G.B. & McCartney, M.P. (2012) Flood pulsing in the Sudd wetland: analysis of seasonal variations in inundation and evaporation in South Sudan. *Earth Interactions*, 16, 1–19.
- Rodell, M., Houser, P., Jambor, U., Gottschalck, J., Mitchell, K., Meng, C.-J. et al. (2004) The global land data assimilation system. *Bulletin of the American Meteorological Society*, 85, 381–394.
- van der Schalie, R., Preimesberger, W., Pasik, A. & Scanlon, T. (2023) ESA Climate Change Initiative Plus Soil Moisture Product User Guide (PUG) Supporting Product Version v08.1 (V1.0 Issue 1.0). <https://doi.org/10.5281/zenodo.8320914>.
- Schwingshackl, C., Hirschi, M. & Seneviratne, S.I. (2017) Quantifying spatiotemporal variations of soil moisture control on surface energy balance and near-surface air temperature. *Journal of Climate*, 30, 7105–7124.
- Spengler, T. & Smith, R.K. (2008) The dynamics of heat lows over flat terrain. *Quarterly Journal of the Royal Meteorological Society: A Journal of the Atmospheric Sciences, Applied Meteorology and Physical Oceanography*, 134, 2157–2172.
- Stensrud, D.J. (1996) Importance of low-level jets to climate: a review. *Journal of Climate*, 1, 1698–1711.
- Sutcliffe, J. & Brown, E. (2018) Water losses from the Sudd. *Hydrological Sciences Journal*, 63, 527–541.
- Talib, J., Taylor, C.M., Duan, A. & Turner, A.G. (2021) Intraseasonal soil moisture–atmosphere feedbacks on the Tibetan plateau circulation. *Journal of Climate*, 34, 1789–1807.
- Talib, J., Taylor, C.M., Klein, C., Harris, B.L., Anderson, S.R. & Semeena, V.S. (2022) The sensitivity of the west African monsoon circulation to intraseasonal soil moisture feedbacks. *Quarterly Journal of the Royal Meteorological Society*, 148, 1709–1730.
- Talib, J., Taylor, C.M., Harris, B.L. & Wainwright, C.M. (2023) Surface-driven amplification of Madden–Julian oscillation circulation anomalies across East Africa and its influence on the Turkana jet. *Quarterly Journal of the Royal Meteorological Society*, 149, 1890–1912.
- Taylor, C.M. (2015) Detecting soil moisture impacts on convective initiation in Europe. *Geophysical Research Letters*, 42, 4631–4638.
- Taylor, C.M., Parker, D.J. & Harris, P.P. (2007) An observational case study of mesoscale atmospheric circulations induced by soil moisture. *Geophysical Research Letters*, 34(15).
- Taylor, C.M., Gounou, A., Guichard, F., Harris, P.P., Ellis, R.J., Couvreux, F. et al. (2011) Frequency of Sahelian storm initiation enhanced over mesoscale soil-moisture patterns. *Nature Geoscience*, 4, 430–433.
- Taylor, C.M., Birch, C.E., Parker, D.J., Dixon, N., Guichard, F., Nikulin, G. et al. (2013) Modeling soil moisture–precipitation feedback in the Sahel: importance of spatial scale versus convective parameterization. *Geophysical Research Letters*, 40, 6213–6218.
- Teuling, A., Seneviratne, S.I., Williams, C. & Troch, P.A. (2006) Observed timescales of evapotranspiration response to soil moisture. *Geophysical Research Letters*, 33(23).
- Ulaby, F.T. (1982) Microwave remote sensing active and passive. *Radar Remote Sensing and Surface Scattering and Emission Theory*, 3, 848–902.
- Viste, E. & Sorteberg, A. (2013) Moisture transport into the Ethiopian highlands. *International Journal of Climatology*, 33, 249–263.

- Vizy, E.K. & Cook, K.H. (2019) Observed relationship between the Turkana low-level jet and boreal summer convection. *Climate Dynamics*, 53, 4037–4058.
- Wainwright, C.M., Finney, D.L., Kilavi, M., Black, E. & Marsham, J.H. (2021) Extreme rainfall in East Africa, October 2019–January 2020 and context under future climate change. *Weather*, 76, 26–31.
- Walker, D.P., Birch, C.E., Marsham, J.H., Scaife, A.A., Graham, R.J. & Segele, Z.T. (2019) Skill of dynamical and GHACOF consensus seasonal forecasts of east African rainfall. *Climate Dynamics*, 53, 4911–4935.
- Walters, D., Boutle, I., Brooks, M., Melvin, T., Stratton, R., Vosper, S. et al. (2017) The met Office unified model global atmosphere 6.0/6.1 and JULES global land 6.0/6.1 configurations. *Geoscientific Model Development*, 10, 1487–1520.
- Warner, J.L., Petch, J., Short, C.J. & Bain, C. (2023) Assessing the impact of a NWP warm-start system on model spin-up over tropical Africa. *Quarterly Journal of the Royal Meteorological Society*, 149, 621–636.
- Warner, J.L., Munday, C. & Engelstaedter, S. (2024) Resolving the Turkana jet-impact of model resolution in simulating channel flow and inversions. *Journal of Geophysical Research: Atmospheres*, 129, e2023JD040299.
- White, J.D., Aiyyer, A. & Russell, J.O. (2021) The impact of orography on the African easterly wave stormtrack. *Journal of Geophysical Research: Atmospheres*, 126, e2020JD033749.
- Young, H.R. & Klingaman, N.P. (2020) Skill of seasonal rainfall and temperature forecasts for East Africa. *Weather and Forecasting*, 35, 1783–1800.

SUPPORTING INFORMATION

Additional supporting information can be found online in the Supporting Information section at the end of this article.

How to cite this article: Talib, J., Taylor, C.M., Klein, C., Warner, J., Munday, C., Folwell, S. *et al.* (2025) Modelling the influence of soil moisture on the Turkana jet. *Quarterly Journal of the Royal Meteorological Society*, e4972. Available from: <https://doi.org/10.1002/qj.4972>